REPORT DOCUMENTATION PAGE

1. AGENCY USE ONLY *(Leave Blank)*	2. REPORT DATE	3. REPORT TYPE AND DATES COVERED
	March 1996	Final Technical Report 010992 - 290296

4. TITLE AND SUBTITLE

Damage and Failure Behavior of SiC SCS-6/Timetal 21S Metal Matrix Composite

5. FUNDING NUMBERS

FQ8671-9201544 2302/BS

92-C-0063

6. AUTHOR(S)

D. A. Shockey, S. W. Kirkpatrick, C. G. Schmidt, and T. Kobayashi

7. PERFORMING ORGANIZATION NAME(S) AND ADDRESS(ES)

SRI International
333 Ravenswood Avenue
Menlo Park, CA 94025-3493

8. PERFORMING ORGANIZATION

AFOSR-TR-96

0250

9. SPONSORING / MONITORING AGENCY NAME(S) AND ADDRESS(ES)

Air Force Office of Scientific Research
Building 410, Bolling AFB
Washington, DC 20332-6448

N/A

AGENCY REPORT NUMBER

F49620-92-C-0063

11. SUPPLEMENTARY NOTES

12a. DISTRIBUTION / AVAILABILITY STATEMENT

UNCLASSIFIED/UNLIMITED

12b. DISTRIBUTION CODE

19960523 195

13. ABSTRACT *(Maximum 200 words)*

SRI International is performing a program of research to (1) determine the microstructural mechanisms underlying failure of metal matrix composites (MMCs), (2) measure the deformation and failure properties of MMCs under combined loading conditions, and (3) develop computational models for deformation and failure. In addition, we are helping the Wright Laboratory determine the microfailure sequence in a brittle matrix composite (BMC). This report describes the results obtained under Phase 1 of the research effort. The work will be completed in Phase 2 and reported in detail in a more comprehensive technical report.

We quantified and analyzed the topography of fracture surfaces to reconstruct the fracture process and delineate the sequence of microfailure events occurring in SCS-6/Timetal 21S MMC under tensile load at room and elevated temperatures and under thermomechanical fatigue conditions. We performed a similar analysis on a SiC-fiber-reinforced borosilicate glass BMC tested at elevated temperature at the Wright Laboratory.

14. SUBJECT TERMS			15. NUMBER OF PAGES
Metal Matrix Composites	SiC Fiber	Fracture Surface Analysis	55
Mechanical Properties	Titanium Alloy	SCS-6	
	Tensile Test	Timetal 21S	16. PRICE CODE

| 17. SECURITY CLASSIFICATION OF REPORT	18. SECURITY CLASSIFICATION OF THIS PAGE	19. SECURITY CLASSIFICATION OF ABSTRACT	20. LIMITATION OF ABSTRACT
UNCLASSIFIED	UNCLASSIFIED	UNCLASSIFIED	UL

CLASSIFIED BY :

N/A since Unclassified.

DECLASSIFY ON :   N/A since Unclassified.

13. ABSTRACT (Continued)

We formulated a three-dimensional model to describe the biaxial behavior of the above composite. Our model is based on an approach similar to the generalized method of cells model. We designed our model to be implemented in an explicit finite element code. The generalized method of cells model is also being used in this program as a baseline model for comparison and model evaluation. We have begun to perform experiments to measure the deformation and failure behavior of MMCs under multiaxial loads. The SCS-6/Timetal 21S composite material was received from Textron, off-axis and biaxial tensile specimens were machined, and preliminary mechanical testing has been performed. We expect to complete the testing and analysis in Phase 2 of the research effort.

DISCLAIMER NOTICE
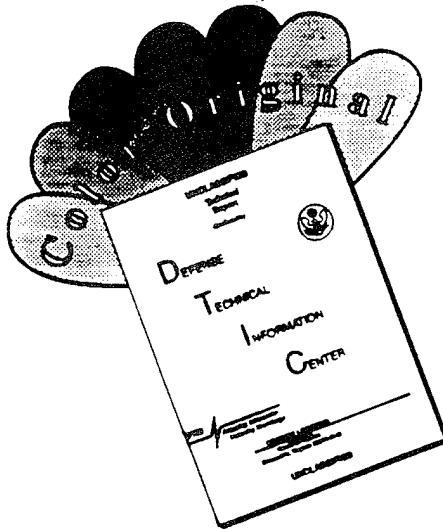
THIS DOCUMENT IS BEST QUALITY AVAILABLE. THE COPY FURNISHED TO DTIC CONTAINED A SIGNIFICANT NUMBER OF COLOR PAGES WHICH DO NOT REPRODUCE LEGIBLY ON BLACK AND WHITE MICROFICHE.

CONTENTS

iv

LIST OF FIGURES

SECTION 1

INTRODUCTION

Composite materials consisting of strong fibers embedded in a ductile matrix are increasingly being considered for advanced aerospace applications like engine rotors in which enhanced strength and stiffness at elevated temperatures are required. The mechanical properties of such metal matrix composites (MMC) depend on their microstructure (the size, type, and volume fraction of the fibers; the composition, grain structure, and thermal mechanical condition of the matrix; and the condition of the fiber-matrix interface), which in turn depends on the fabrication process and, in the application, determines the deformation and failure behavior. Thus, optimization of an MMC microstructure for a given application condition requires an understanding of how microstructural variables affect response to loads, and how fabrication procedures affect microstructure.

The goal of this research program is to advance the current understanding of the deformation and failure behavior of MMCs under uniaxial and multiaxial loading and describe this behavior in the form of a constitutive model that can be incorporated into a three-dimensional finite element code. The model/code capability is intended to provide a way to interrogate the effects of variable fabrication parameters on microstructure, and the effects of microstructure parameters on load response. Such a capability will reduce the number of fabrication trials and mechanical behavior tests required to develop MMCs with properties that meet the specifications for given applications.

To establish the micromechanics of failure and the role of microstructural features on failure, we applied an advanced fractographic technique to specimens of MMCs broken in simple tensile tests and thermomechanical fatigue tests, and to a brittle matrix composite broken under tensile loading at an elevated temperature. By quantifying and comparing the topographies of conjugate fracture surfaces, the mechanisms and sequence of microfailure in SES-6/Timetal 21S and in a silicon carbide fiber-reinforced borosilicate glass were examined.

To investigate the effect of off-axis and multiaxial loads on deformation and failure behavior of the MMC, we designed specimens and testing fixtures that allow application of loads

1

that produce three-dimensional stress states and began to perform failure tests. This testing will be continued and concluded in the Phase 2 effort.

The understanding and the material behavior data obtained from the fractographic analyses and multiaxial load tests is being used to develop a model that describes deformation and failure of MMCs. The model will be completed in Phase 2. In this final report, we describe work accomplished in Phase 1.

SECTION 2

FRACTURE SURFACE ANALYSES OF TENSILE SPECIMENS

2.1 INTRODUCTION

Tensile specimens of SCS6/Timetal 21-S composite were provided by the University of Dayton Research Institute (UDRI) for fracture surface analysis and model development. Tensile specimens with composite lay-ups of $[0]_4$, $[0/90]_s$, and $[0/\pm 45/90]_s$ that were tested at 23°, 500°, 650°, and 815°C were received with stress-strain curves obtained by UDRI. Table 2.1 summarizes the test conditions and tensile results for the specimens received. This table includes all specimens tested by UDRI that were provided for this investigation.

2.2 RESULTS

2.2.1 Fracture Surface Examination

Figures 2.1 and 2.2 show scanning electron microscope (SEM) micrographs of fracture surfaces from $[0]_4$ tensile specimens tested at 23° and 815°C, respectively. The fracture surface of the matrix component of the specimen tested at 23°C (Figure 2.2) exhibits the features of a material that failed in a ductile manner; however, in one of the composite plies, remnants of a molybdenum woof fiber is clearly evident (see Figure 2.1e). Evidence of the fiber appears on both sides of the fracture surface. An X-ray energy dispersive spectrometer (EDS) analysis of the woof fiber indicated that its composition is high in molybdenum (see Table 2.2). The measured compositions of the matrix and the fiber are consistent with the nominal compositions of Timetal 21-S and SiC, respectively.

The appearance of the matrix material on the fracture surface of the $[0]_4$ tensile specimen tested at 815°C shows greater ductility than the fracture surfaces from the 23°C test. To better compare the differences between the specimens tested at these two temperatures, a scanning laser microscope was used to topographically characterize representative regions of the fracture surfaces from tensile specimens tested at 23° and 815°C, as shown in Figure 2.3. Figure 2.4 compares the fracture surface profile of the matrix material between two fibers in 23° and 815°C test specimens. The fracture surfaces of the matrix from the 23°C test are relatively flat and at an angle that

3

Table 2.1

SCS6/TIMETAL 21-S COMPOSITE TENSILE TEST DATA

Specimen Designation	Lay-up	Area mm²	Test Temperature °C	Room Temperature Modulus GPa	Test Temperature Modulus GPa	Yield Strength MPa	Maximum Tensile Strength MPa	Elongation to Failure %	Fracture Surface Available for Analysis
91-253	[0]4	4.6626	23	209.6	209.6	1307	2005	1.7	no
91-254	[0]4	4.7782	23	197.1	197.1	1853	1983	1.4	yes
91-250	[0]4	6.0632	500	222.2	189.7	not available	1487	0.94	yes
91-251	[0]4	6.0393	500	215.3	194.1	not available	1449	0.88	yes
91-249	[0]4	6.0871	500	214.6	187.9	not available	1399	0.88	yes
91-252	[0]4	6.0632	650	231.6	175.7	1141	1141	0.86	yes
91-248	[0]4	6.0632	650	194.0	185.7	1083	1203	0.94	yes
91-247	[0]4	6.0632	815	not available	135.0	not available	936	0.79	yes
91-220	[0/90]s	4.7264	23	154.2	154.2	882.4	1135.7	1.14	yes
91-219	[0/90]s	9.4768	23	156.1	156.1	911.8	1042.6	0.96	no
91-216	[0/90]s	6.0393	500	178.4	120.0	865.5	882.7	0.94	yes
91-215	[0/90]s	11.9832	500	187.1	120.4	864.3	885.7	0.93	yes
91-217	[0/90]s	6.0393	650	164.3	106.9	623.9	644.1	0.85	no
91-214	[0/90]s	12.0071	650	165.5	136.7	495.9	630.6	0.89	yes
91-218	[0/90]s	6.2516	815	not available	124.8	394.0	495.0	0.75	no
91-213	[0/90]s	11.9593	815	not available	116.2	334.5	480.0	0.97	yes
91-288	[0/±45/90]s	9.2129	23	141.8	141.8	593.9	783.5	0.97	yes
91-287	[0/±45/90]s	18.0645	23	156.4	156.4	not available	did not fail	did not fail	no
91-284	[0/±45/90]s	11.4406	500	155.0	120.0	575.9	598.3	0.74	yes
91-283	[0/±45/90]s	22.4806	500	165.2	124.9	592.2	645.9	0.79	yes
91-286	[0/±45/90]s	11.6516	650	158.2	121.8	329.1	436.6	0.76	yes
91-282	[0/±45/90]s	22.8516	650	162.4	128.4	335.6	466.0	0.88	no
91-281	[0/±45/90]s	22.5251	650	160.2	111.6	367.9	436.2	not available	no
91-285	[0/±45/90]s	11.8180	815	not available	110.6	207.2	314.7	0.73	no
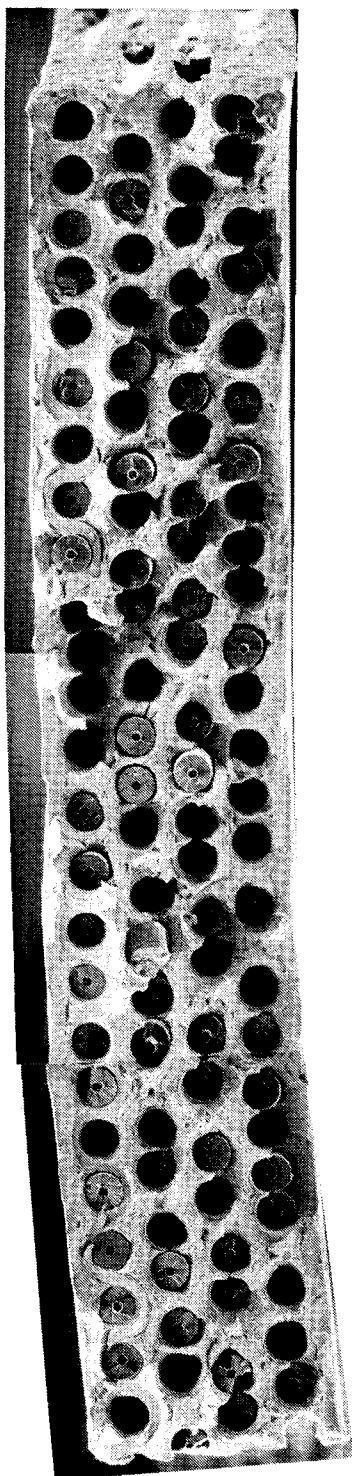
(a) Side A
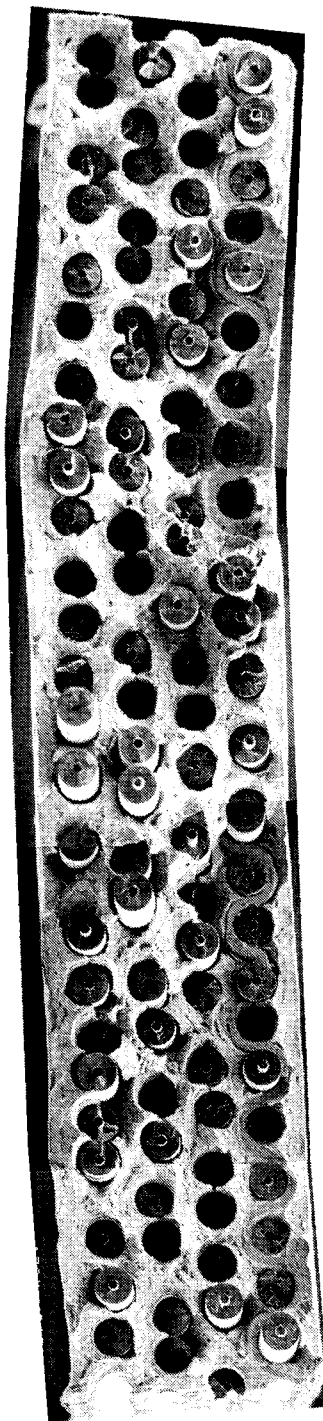
(b) Side B

100 μm

CPM-3894-1

Figure 2.1. SEM micrographs of the fracture surfaces from the 23°C tensile test of Specimen 91-254.
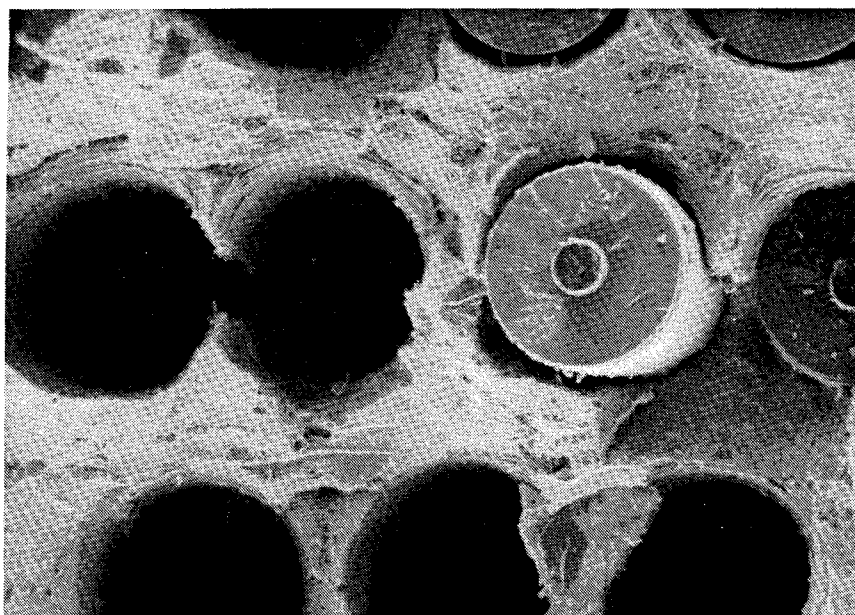
(c) Orthogonal high magnification view of area on Side A
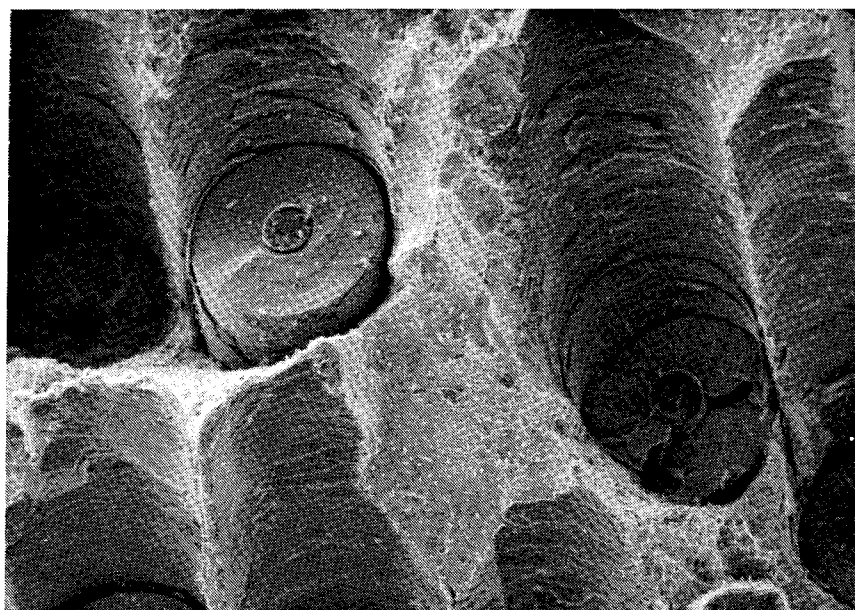
(d) Angled high magnification view of area on Side A

├─────┤
50 μm

CPM-3894-2

Figure 2.1. SEM micrographs of the fracture surfaces from the 23°C
tensile test of Specimen 91-254. (Continued)

6
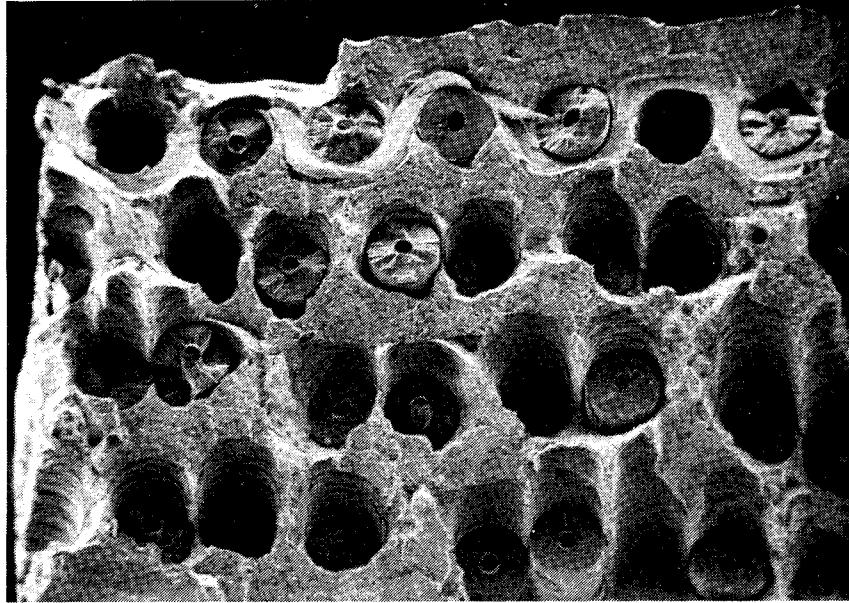
(e) High magnification view showing molybdenum fiber

⌞   ⌟
100 µm

CPM-3894-3

Figure 2.1. SEM micrographs of the fracture surfaces from the 23°C
tensile test of Specimen 91-254. (Concluded)
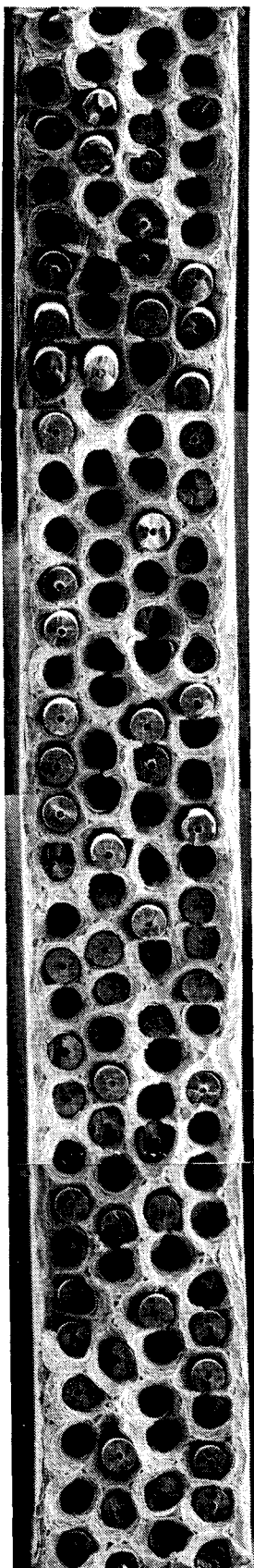
(a) Side A
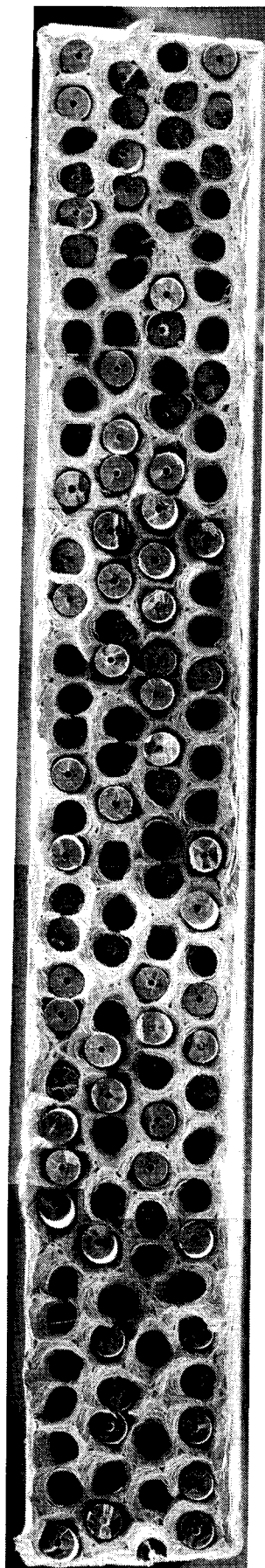
(b) Side B

100 μm

CPM-3894-4

Figure 2.2. SEM micrographs of the fracture surfaces resulting from the 815°C tensile test of Specimen 91-247.
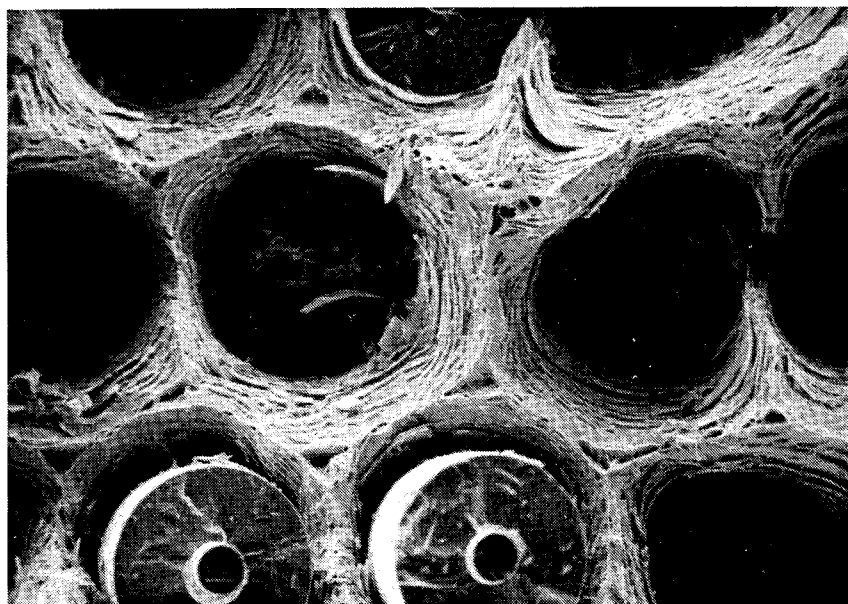
(c) Orthogonal high magnification view of area on Side A
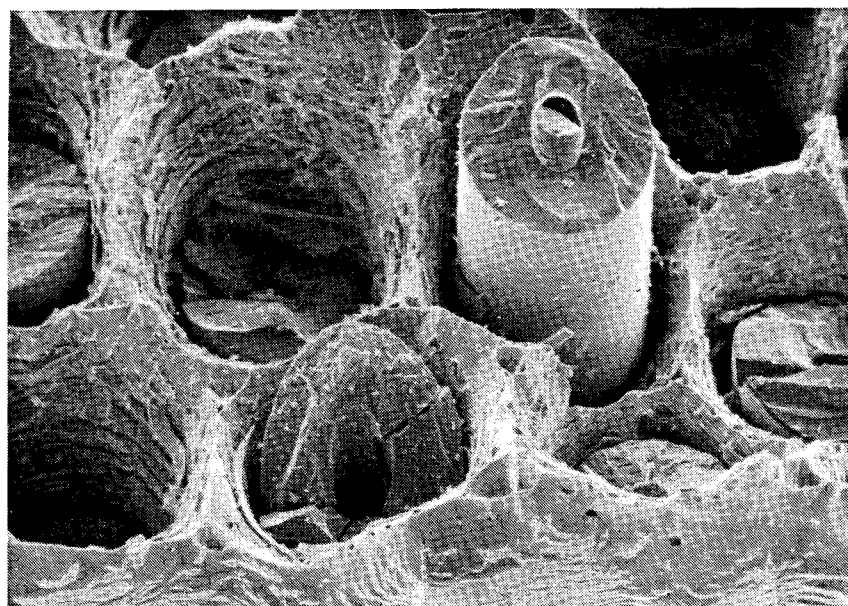
(d) Angled high magnification view of area on Side A

50 µm

CPM-3894-5

Figure 2.2.   SEM micrographs of the fracture surfaces resulting from the
815°C tensile test of Specimen 91-247. (Concluded)

Table 2.2

TYPICAL COMPOSITIONS OF THE WOOF FIBER, MATRIX, AND SiC FIBER ON THE FRACTURE SURFACE OF SPECIMEN 91-254

Location	Composition (Weight Percent)			
	Ti	Si	Mo	Al
Woof Fiber	15.0	1.9	82.4	0.8
Matrix	84.1	1.7	13.6	0.6
SiC Fiber	0.6	92.4	5.3	1.6
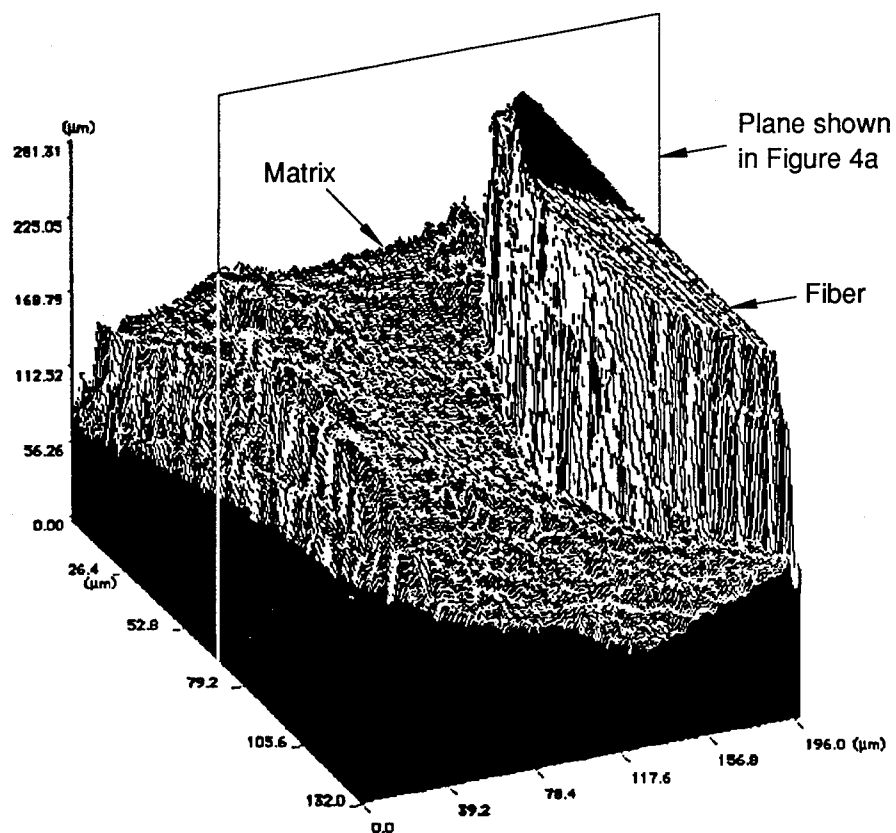
(a) Top fracture surface profile in Figure 4a (23°C test; Specimen 91-254)
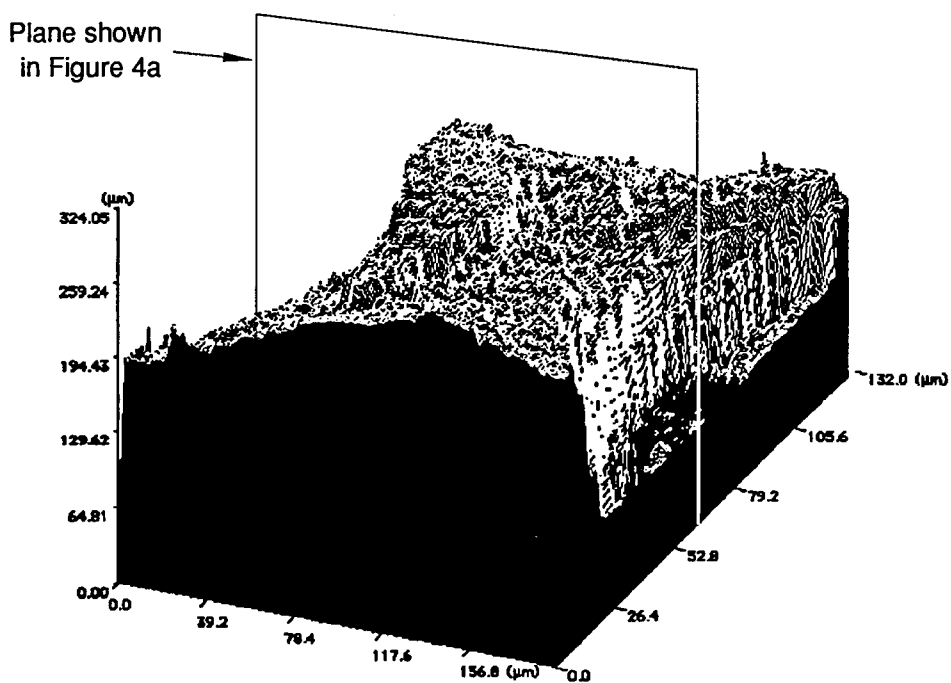
(b) Bottom fracture surface profile in Figure 4a (23°C test; Specimen 91-254)

CM-3894-6

Figure 2.3.   Fracture surface profiles measured with a scanning laser microscope.

11
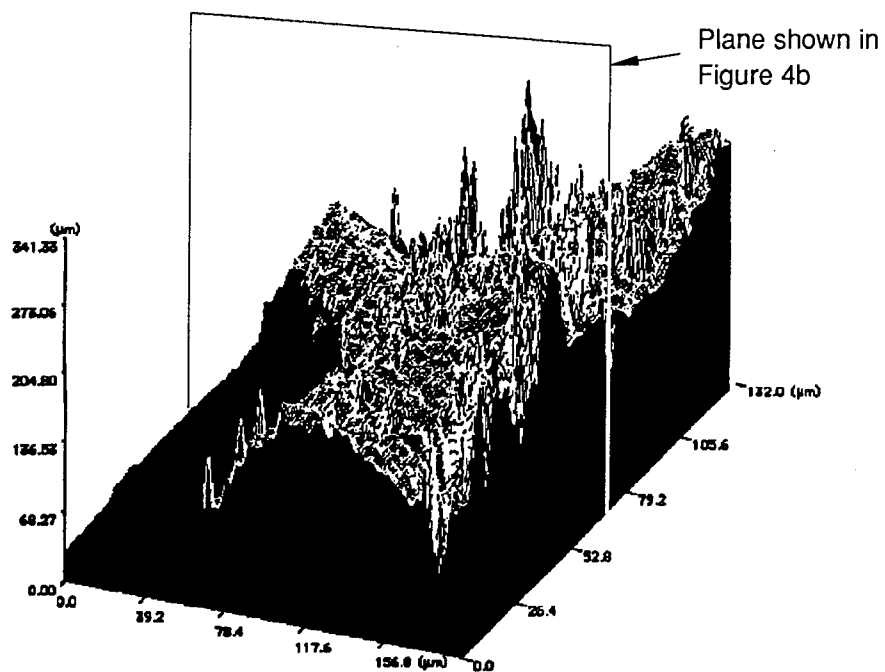
(c) Top fracture profile in Figure 4b (815°C test; Specimen 91-247)
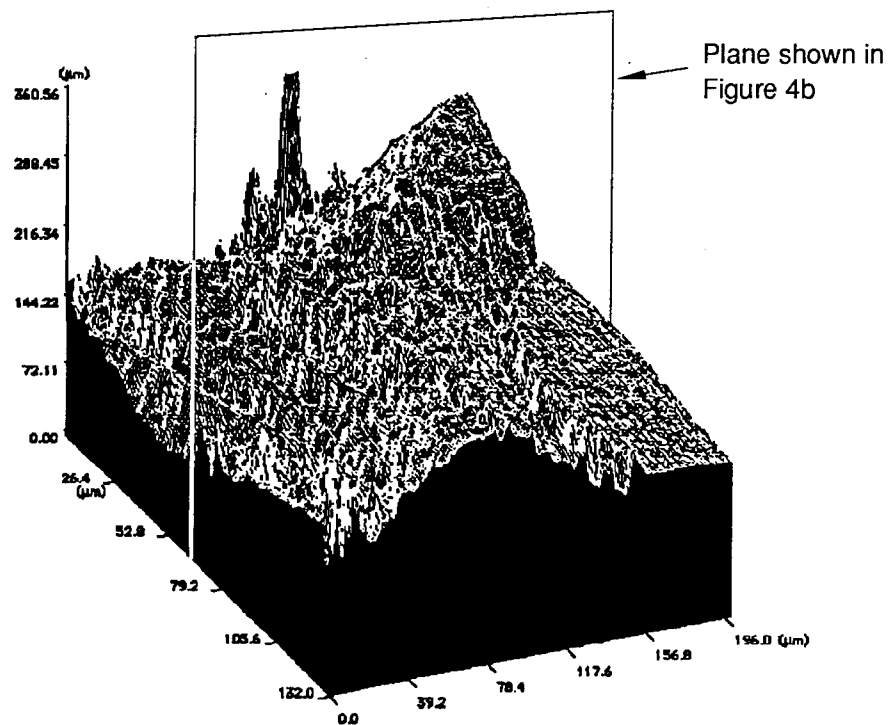
(d) Bottom fracture surface profile in Figure 4b (815°C test; Specimen 91-247)

CM-3894-7

Figure 2.3.   Fracture surface profiles measured with a scanning laser
microscope. (Concluded)

12
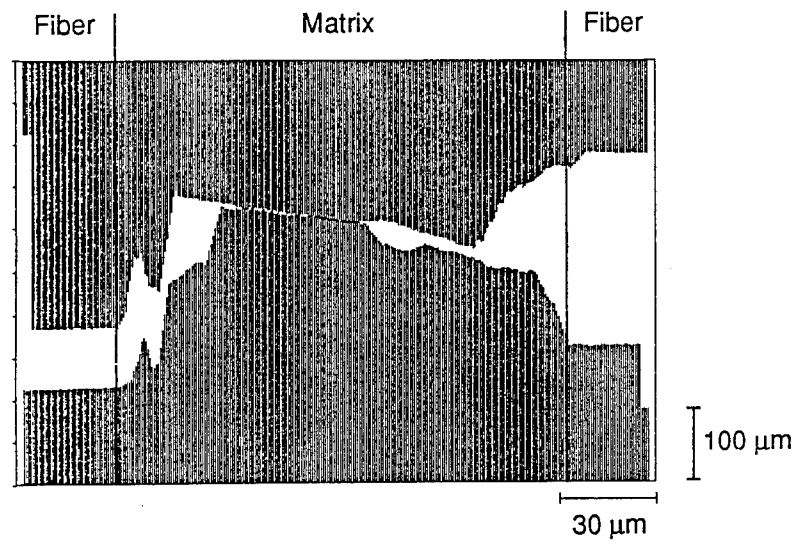
(a) 23°C Test; Specimen 91-2154
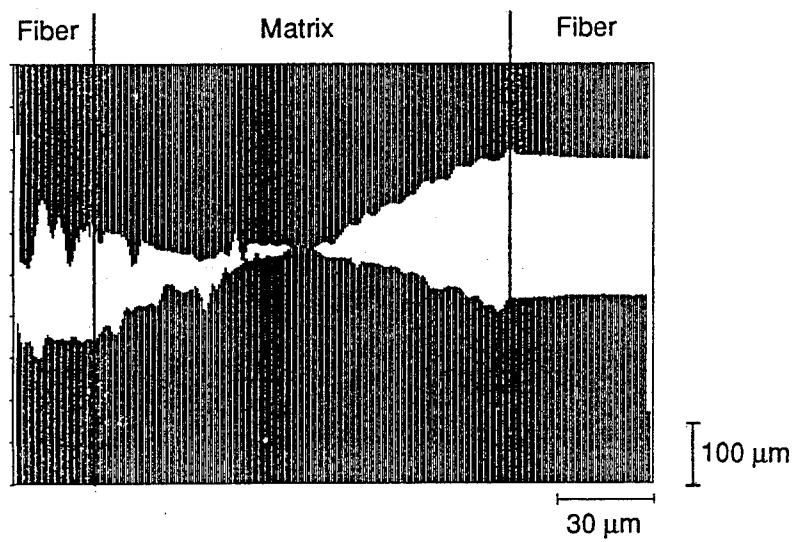
(b) 815°C Test; Specimen 91-247

CA-3894-8

Figure 2.4. Conjugate fracture surface profile from [0]₄ tensile test specimens.

suggests a ductile shear dominated failure process. The fracture surface of the matrix material in the 815°C test indicates a ductile necking type of failure.

2.2.2 Stress-Strain Behavior Examination

An analysis of the stress-strain behavior was undertaken to assist in determining the significance of the fractographic features. Through the analysis described below, we concluded that the fracture surface features strongly reflect the matrix deformation that occurs after the maximum stress is reached. The magnitude of the maximum stress is primarily determined by the fiber strength and the nonelastic deformation of the matrix.

Figure 2.5 compares the stress-strain responses of several $[0]_4$ and $[0/90]_s$ tensile test specimens that were examined in this investigation. To estimate the contribution of the matrix and the fibers to the stress-strain behavior of the tests on the $[0]_4$ composite shown in Figure 2.5a, an isostrain rule-of-mixtures (ROM) approach was employed, with no bonding between the fibers and the matrix. This approach is consistent with that used by Larsen and Nicholas[1] and by Neu and Nicholas[2] in their analysis of thermomechanical fatigue of SCS6/Timetal 21-S composites. We assumed that no damage (i.e., cracking) occurs to the matrix during loading until the maximum load is reached. The stress-strain behavior of the Timetal 21-S matrix material was determined from a version of the Bodner-Partom model developed by Neu.[3] Figure 2.6 shows calculations of the fraction of the load borne by the fibers in $[0]_4$ composite tensile tests at various temperatures.

These ratios were determined by subtracting the matrix contribution obtained from Neu's model from the measured stress-strain behavior of the composite and dividing this difference by the measured stress-strain behavior of the composite. Figure 2.6 shows that the fibers bear a majority of the load in all cases (i.e., a little more than 60% of the load at 23°C and as much as 93% of the load at 815°C).

---

[1] J. M. Larsen and T. Nicholas, "Mechanical Behavior and Damage Tolerance and Titanium Matrix Composites," overview presentation of work performed by Wright Laboratory Materials Directorate in Government Work Package (GWP) 85.

[2] R. W. Neu and T. Nicholas, "Effect of Laminate Orientation on the Thermomechanical Fatigue Behavior of a Titanium Matrix Composite," Journal of Composites Technology and Research, 16(3), 214-224 (1994).

[3] R. W. Neu, "Nonisothermal Material Parameters for the Bodner-Partom Model," paper presented at the Symposium on Parameter Estimation for Modern Constitutive Equations, ASME Winter Annual Meeting, Nov. 28 - Dec. 3, 1993, New Orleans, LA.

(a) [0]₄ composite
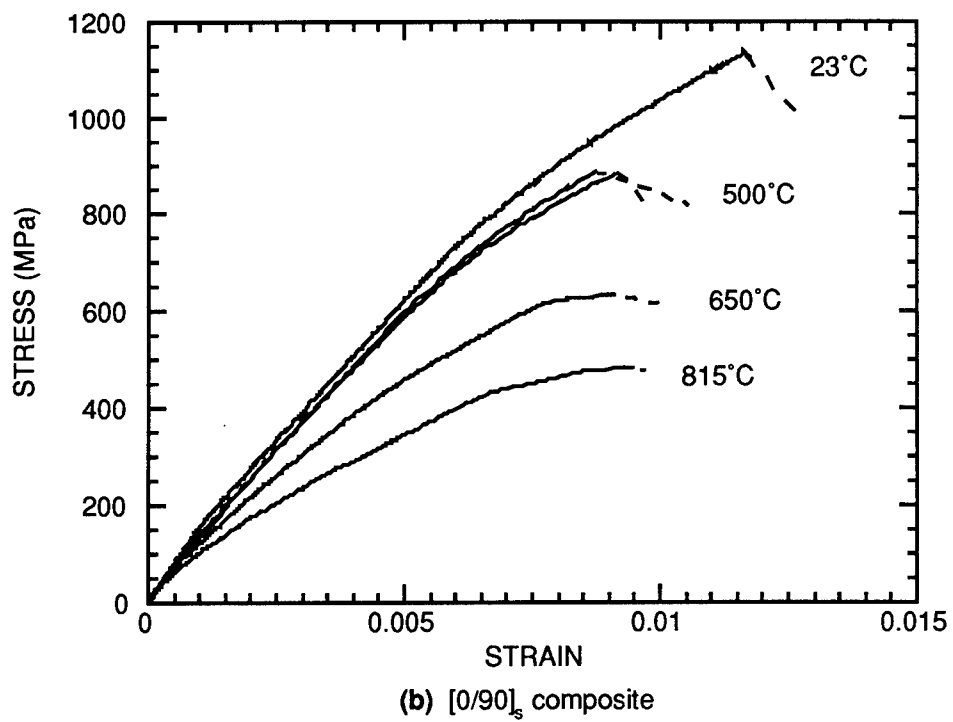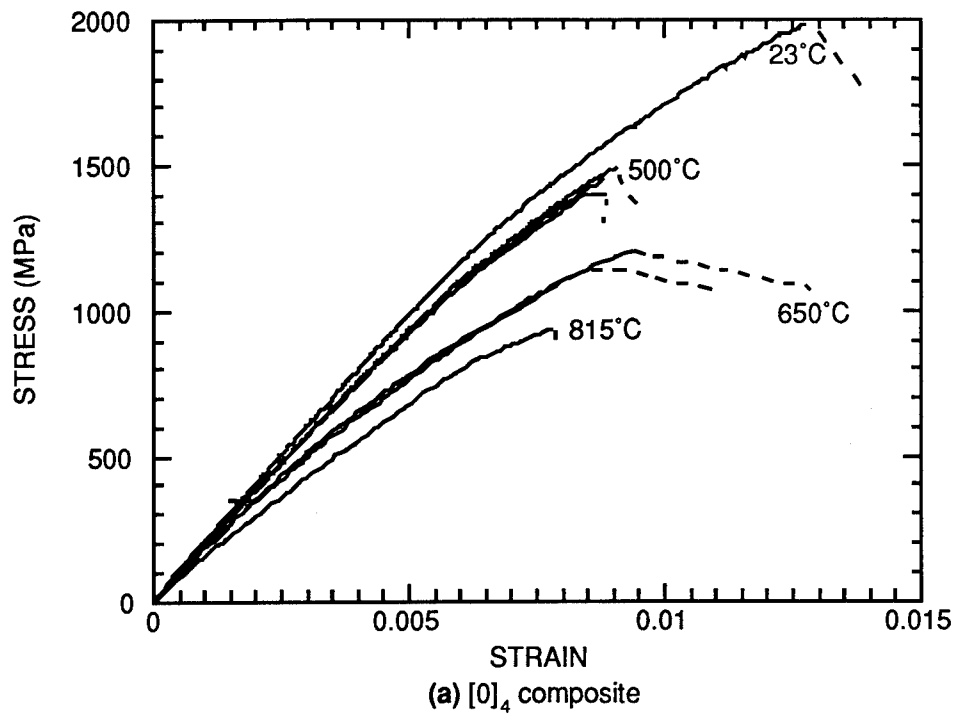
(b) [0/90]ₛ composite

CM-3894-9

Figure 2.5.   Stress-strain curves for SCS6/Timetal 21-S composite.

15

$$P_{fiber}/P_{total\ composite} = 1 - \sigma_{matrix} * (1-V_f) / \sigma_{total\ composite}$$
where
σ_{matrix} is determined from Neu's model and
V_f is the volume fraction of the fiber (= 0.36).
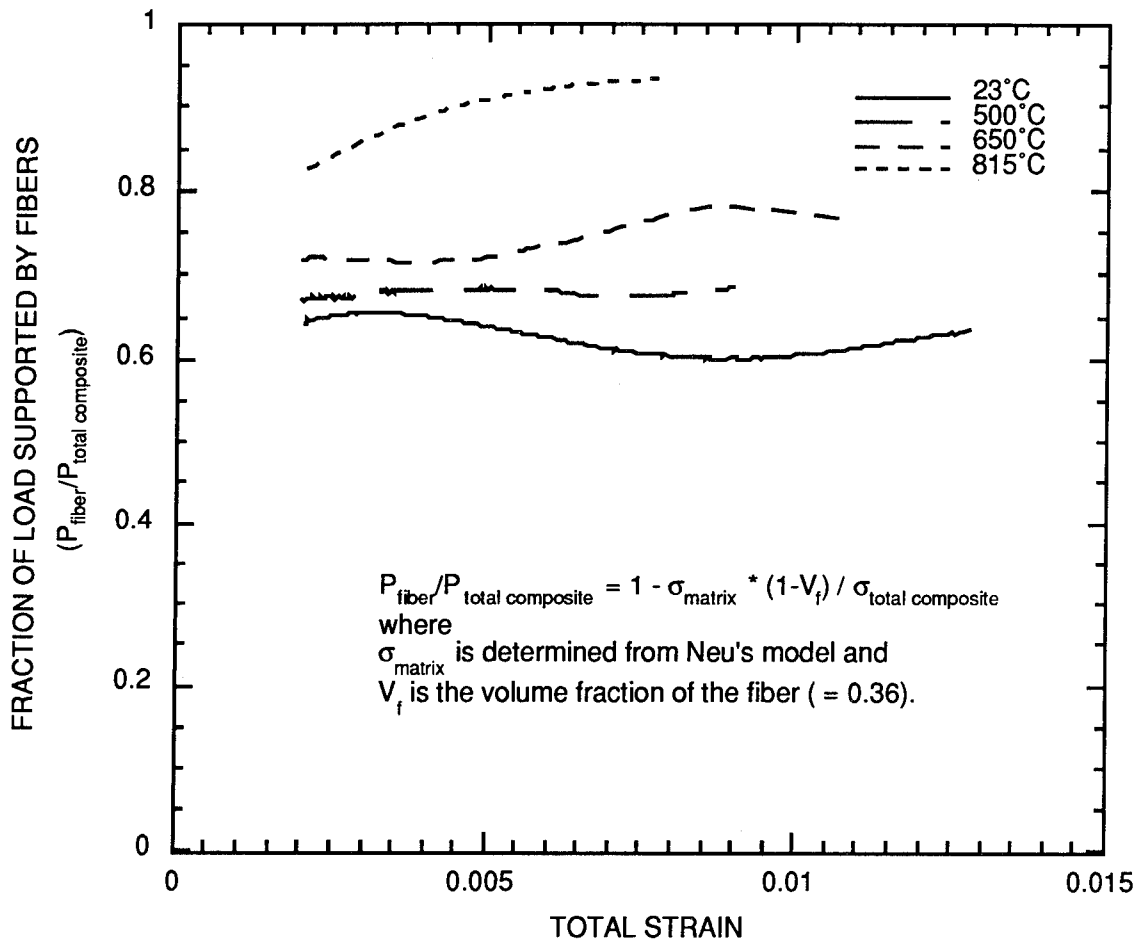
CM-3894-10

Figure 2.6.   Fraction of the load supported by fibers in tensile tests on $[0]_4$ SCS6/Timetal 21-S composite.

A prediction of the stress-strain response of the $[0/90]_s$ composite was produced that was based on the following assumptions:

- The bond strength between the fiber and the matrix is negligible.

- The matrix is not damaged (i.e., does not crack) until after the maximum load is reached.

- The isostrain ROM model is valid for the conditions examined.

- The contribution of the 90° plies to the strength of the composite is from the matrix outside the volume of material described by the plane of fibers and their thickness.

The fiber strength used in the model was computed from the observed $[0]_4$ behavior and the matrix strength computed from Neu's model. The predicted stress in the $[0/90]$ composites was calculated as follows.

$$\sigma[0/90]_s = \frac{\sigma[0]_4}{2} + 2 * \sigma[90] \qquad (1)$$

where $\sigma[0]_4$ = measured stress in the $[0]_4$ composite specimen tests

$\sigma[90]$ = calculated stress in a 90° ply of the $[0/90]_s$ composite

$\qquad (= [d_{ply} - d_{fiber}] / d_{ply} * \sigma_{matrix})$

d_{ply} = thickness of the 90° ply (= 0.238 mm)

d_{fiber} = fiber diameter (= 0.140 mm)

σ_{matrix} = matrix stress computed from Bodner-Partom model.

Figure 2.7 compares the predictions and the measured values of stress in the $[0/90]_s$ tensile tests up to the maximum stress. The comparison shows very good agreement.

2.3 DISCUSSION

The observation that matrix damage is preceded by fiber breakage is similar to the findings of others who have studied similar composites. Majumdar and Newaz[4] investigated the tensile properties of SCS6/Ti-15-3 composites with [0] and [90] fiber orientations. The Ti-15-3 alloy is about 25% weaker than Timetal 21-S but shares the characteristics of high ductility and weak

---

[4] B. S. Majumdar and G. M. Newaz, "Inelastic Deformation of Metal Matrix Composites: Plasticity and Damage Mechanisms," Phil. Mag. A, **66**(2), 187-212 (1992).

17
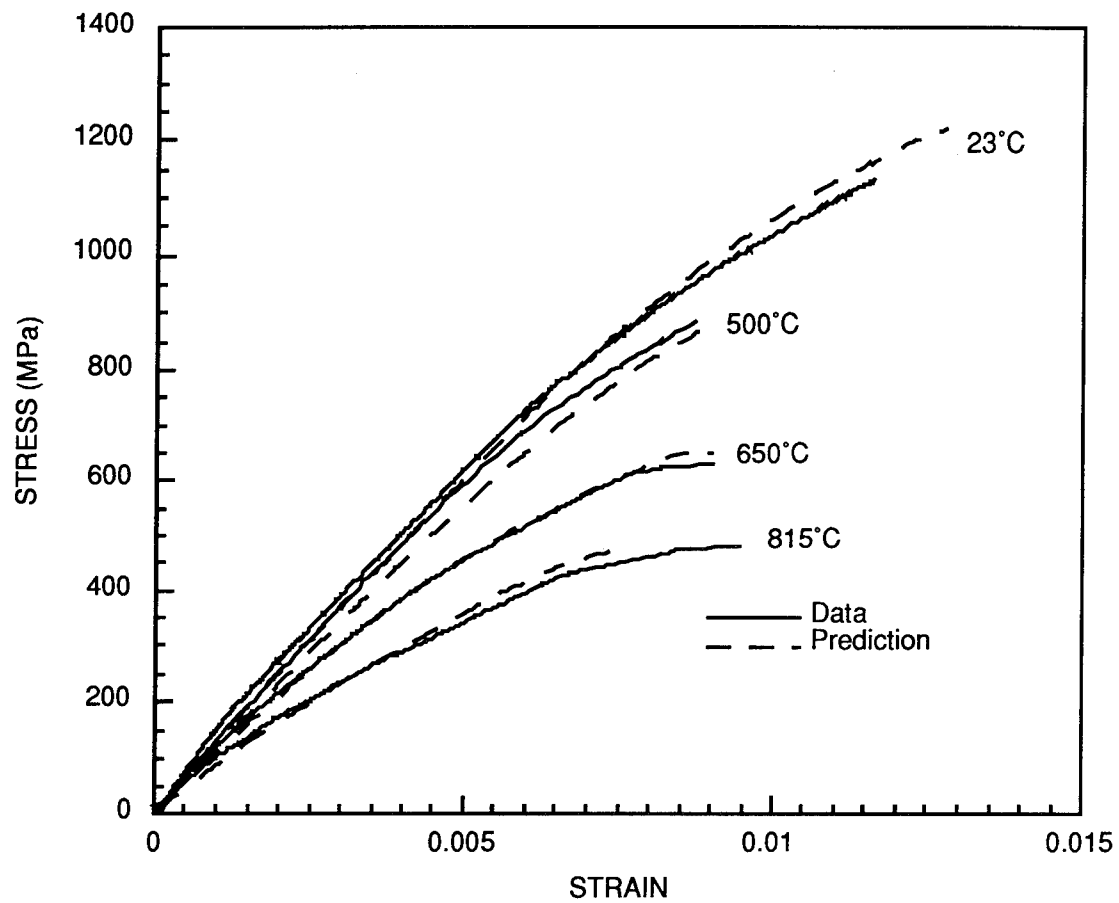
Figure 2.7. Comparison of measured and predicted stress-strain behavior for [0/90]$_s$ SCS6/Timetal 21-S composite based on [0]$_4$ data and Neu's model for Timetal 21-S.

bonding to SCS6 fibers. Majumdar and Newaz found that damage (i.e., cracking) in the [0] composite prior to the maximum load was generally confined to small cracks in the fiber/matrix interface that did not propagate into the fiber or the matrix. Also, Lerch[5] found extensive deformation but no cracks in the matrix of $[0]_4$ specimens strained just short of the maximum load in a SCS6/Ti-15-3 composite. He reported the presence of matrix cracks only in composites with 30° plies.

Jeng, Yang, and Yang[6] and Yang and Jeng[7] classified the tensile behavior in a range of titanium alloy composites and found that the toughness of the matrix and the fiber strength/interface strength ratio were the most important variables. Although they did not report results on SCS6/Timetal 21-S, they did study titanium alloy composites with similar properties (i.e., composites with a high matrix toughness and a high fiber-to-interface strength ratio, such as the SCS6/Ti-15-3 composite in the as-received condition). They state that in such cases tensile loading of $[0]_4$ composites initiates cracking in the interface layer. These cracks are arrested by microyielding of the matrix but produce limited interfacial debonding between the matrix and the fiber on further loading. The remaining interfacial bonds are strong enough to transfer load back into the interfacial zone and continue to fracture the interface. Fracture of the composite is initiated by fiber fracture, which, in turn, occurs at randomly distributed weak spots in the fibers.

The present results fit the descriptive model of Jeng, Yang, and Yang in at least two respects: (1) damage (i.e., cracking) that occurs during loading is confined to a small region of the composite (the fiber/matrix interface), and (2) the failure of the fibers precedes matrix failure in the final stages of failure of the composite.

The observations that the final stages of composite fracture are initiated by the fibers and that the fibers carry most of the load have important implications for the analysis of the fracture surfaces. These observations suggest that the observable matrix fracture features reflect the failure processes occurring in the matrix after fiber failure. The loads that can be sustained by the matrix are small compared with those supported by the fibers, and the ductility of the matrix is significantly greater, so matrix fracture occurs after the maximum load of the composite is reached. Consequently, the matrix fracture surfaces that are observed reflect failure processes that occur in the final stage of composite failure in a tensile test. Detailed reconstruction of the fracture

[5] B. A. Lerch, "Matrix Plasticity in SiC/Ti-15-3 Composite," NASA Report No. NASA-TM-103760, July 1991.
[6] S. M. Jeng, J.-M. Yang, and C. J. Yang, "Fracture Mechanisms of Fiber-Reinforced Titanium Alloy Matrix Composites. Part II; Tensile Behavior," Materials Science and Engineering, **A138**, 169-180 (1991).
[7] J.-M. Yang and S. M. Jeng, "Deformation and Fracture of Ti-and Ti₃Al-Matrix Composites," Journal of Metals, pp. 52-57 (June 1992).

process—by fracture surface topography analysis (FRASTA), for example—will be strongly influenced by the matrix failure processes that occur immediately before final failure and only weakly influenced by the initiation and early stages of the failure process. The fact that no extraordinary stress-strain behavior was observed when a physically large inhomogeneity (the woof fiber) was present on the fracture surface also implies that the tensile behavior of the particular composite is not sensitive to the matrix behavior.

2.4 SUGGESTIONS FOR FUTURE RESEARCH

The weak correlation between tensile properties and fracture surface topography is not likely to persist in specimens subjected to other forms of loading. Thermomechanical loading is known to involve an interplay between matrix dominated behavior and fiber dominated behavior. For example, Mall et al.[8] found that out-of-phase thermal and mechanical cyclic conditions produced failures that were matrix dominated, whereas fiber dominated behavior was observed under in-phase or isothermal conditions. Different heat treatment conditions can also profoundly affect the role of the matrix, interface, and fiber. Yang and Jeng[7], for example, found that interface conditions and fiber strength could be altered by heat treatment of the composite so that matrix dominated or fiber dominated failures would result.

To fully exploit the capabilities of quantitative fracture surface analysis in understanding the role of the matrix, fiber, and interface in determining the mechanical properties of SCS6/Timetal 21-S composites, we recommend that fracture surface analyses focus on fatigue loading, material condition variables, and, perhaps, environmental variables. An understanding of conditions where matrix failure plays a dominant or at least a significant role in determining composite behavior will enable conclusions to be drawn about the initiation and development of failures in SCS6/Timetal 21-S composites and hence provide the basis for tailoring these materials to specific aerospace applications.

2.5 SUMMARY

The following inferences can be drawn as a result of the accurate predictions of the $[0/90]_s$ stress-strain curves and the results of analyses of the $[0]_4$ composite:

---

[8] S. Mall, D. G. Hanson, T. Nicholas, and S. M. Russ, "Thermomechanical Fatigue Behavior of a Cross-Ply SCS-6/β21-S Metal Matrix Composite," in *Constitutive Behavior of High Temperature Composites*, MD-Vol. 40, B. S. Majumdar, G. M. Newaz, and S. Mall, Eds. (American Society of Mechanical Engineers, New York, 1992), pp. 91-106.

- Failure of the matrix occurs after the maximum load is reached and after some or all of the 0° fibers have failed, as implied by the accurate prediction of the stress-strain curve up to the maximum stress by a model that assumes no damage (i.e., cracking) occurred in the matrix.

- Only part of the matrix phase of the 90° plies in a [0/90]$_s$ composite contributes to the tensile strength. The interface strength between the fibers and the matrix is negligible and does not contribute significantly to the strength of the composite. This finding is consistent with the findings of other studies[1,2] of the same composite.

- The topography of the matrix fracture surface is a strong function of processes that occur during the rapid reduction in load after the maximum load. Events in this regime have little, if any, effect on the stress-strain response of the composite.

- The presence of the woof fiber on the fracture surface of the 23°C test of the [0]$_4$ composite appears to have little or no effect on the tensile behavior of that specimen. This conclusion is based on the accurate prediction of the [0/90]$_s$ composite behavior on the basis of results from the [0]$_4$ composite without any allowance for the presence of the woof fiber.

Future fracture surface analyses of the SCS6/Timetal 21-S composites should focus on the effects of fatigue loading, material condition variables, and, perhaps, environmental variables.

SECTION 3

FRACTURE SURFACE ANALYSES OF THERMOMECHANICAL FATIGUE FAILURES

3.1 INTRODUCTION

We examined the fracture surface of a thermomechanically tested titanium alloy matrix composite consisting of silicon carbide fibers (SCS-6) and Timetal 21S beta titanium matrix (Ti-15Mo-3Nb-3Al-0.2Si). The specimen was acquired from a test program conducted at Wright-Patterson AFB.[9] The composite material was fabricated from alternating layers of rolled titanium foils and woven SCS-6 fibers followed by consolidation by hot isostatic pressing. The composite consisted of four unidirectional laminates with the fibers oriented in the direction of the applied stress (i.e., $[0]_4$). The fibers were 140 μm in diameter and the total thickness of the composite was about 0.9 mm, which resulted in a fiber volume fraction of 0.32. The test specimen was 10 mm in width and was heat treated at 621°C for 8 hours before mechanical testing.

Thermomechanical loading was accomplished by axial loading with a servohydraulic load frame and thermal excursions imposed by quartz lamp heating in an air environment. A section of the specimen about 38 mm in length was uniformly heated in this manner. The mechanical load cycle consisted of a symmetric triangular waveform with a maximum stress of 800 MPa (or load of 785 kg), an $R(=P_{min}/P_{max})$ of 0.1, and a cycle time of 180 s. The thermal cycle was triangular with a 180-s cycle time and with a maximum and minimum temperature of 105° and 650°C, respectively. The mechanical and thermal cycles were conducted out-of-phase (i.e., the stress was at a maximum when the temperature was at a minimum and vice versa). The test was run until failure (i.e., complete separation), which occurred at 1414 cycles.

3.2 RESULTS

Figure 3.1 shows a fracture surface of the thermomechanical test specimen. The right side of the fracture surface is dominated by a fatigue-induced, flat fracture surface that extends from the outer surface of the specimen and penetrates toward the center. Neu and Nicholas[2] described the

---

[9] R. W. Neu and T. Nicholas, "Effect of Laminate Orientation on the Thermomechanical Fatigue Behavior of a Titanium Matrix Composite," Jour. of Composites Tech. and Res., **16**, 214 (1994).

1 mm

(a) SEM Micrograph of Fracture Surface.

Ductile Fracture Region

Fatigue Fracture Region

Fibers Surrounded by the Ductile Matrix Fracture
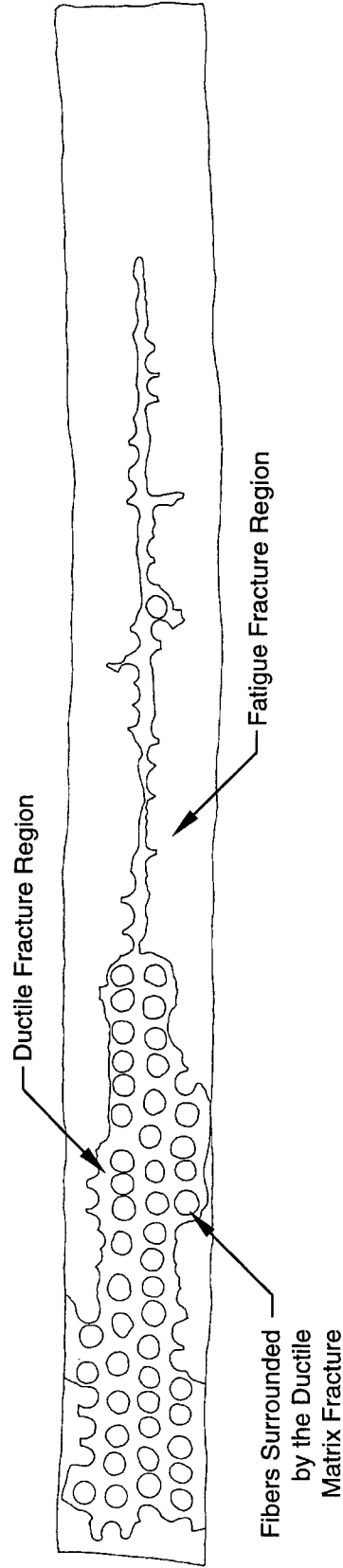
(b) Diagram Showing Regions of Fracture.

CP-3894-1A

Figure 3.1. Fracture surface of thermomechanical test specimen.

24

failure process exhibited by this specimen to be matrix-dominated, because failure initiates in the matrix at the outer surface of the specimen and, with the aid of the environment, propagates through the matrix of the composite. Propagation of the fatigue-induced cracks is incomplete, however, so that a region of ductile rupture is evident between the innermost rows of fibers. It is the ductile fracture regions that fail in the last loading cycle and, therefore, contribute to the residual strength of the composite after fatigue loading. On the left side of Figure 3.1, the region of fatigue-induced fracture features are small so that fracture is dominated by ductile fracture. Figure 3.1b is a map that delineates the ductile and fatigue-induced regions of the fracture surface.

To estimate the contribution of the matrix and the fiber constituents to the residual strength of the composite, we considered the following load paths: (1) fibers that were not broken during thermomechanical fatigue loading, (2) the matrix that did not fail due to thermomechanical fatigue loading, (3) the regions of the matrix that failed in shear as fatigue cracks linked together during the final stages of fracture, and (4) the friction between the matrix and fibers that were broken during fatigue. In the following discussion, we estimate the magnitude of the total load as being the sum of the loads from each of these sources.

As a first estimate, we considered all of the fibers that were surrounded by ductile matrix failure to be unbroken by the thermomechanical fatigue. Figure 3.1b shows the locations of the 48 fibers within the region of ductile matrix failure. Using a fiber strength of 3450 MPa reported by Ward, Herrmann, and Hillberry,[10] we estimate the load supported by the 48 unbroken fibers to be 260 kg.

The area of ductile failure depicted in Figure 3.1b was measured to be 2.28 mm^2. Experimental measurements, reported by Neu,[11] of the tensile properties of similarly processed Timetal 21-S (i.e., so called "neat material") indicate that the maximum stress at 25°C and 500°C is 1150 MPa and 970 MPa, respectively. Interpolating to the temperature where the load was a maximum in the thermomechanical fatigue cycle (i.e., 150°C) indicates that the maximum stress for the matrix was 1050 MPa. This strength value corresponds to a load that is supported by the region of ductile matrix failure shown in Figure 3.1 to be 244 kg.

We used SEM micrograph measurements of the area of shearing to estimate the load required to produce shear failures on the fracture surface. Figure 3.2 shows a side view of the fracture surface displayed in Figure 3.1. Multiple cracks below the ultimate fracture surface are

---

[10] G. T. Ward, D. J. Herrmann, and B. M. Hillberry, NASA Report 191467, July 1993.
[11] R. W. Neu, "Nonisothermal Material Parameters for the Bodner-Partom Model," in Symposium on Parameter Estimation for Modern Constitutive Equations, ASME Winter Annual Meeting, Nov. 28 - Dec. 3, 1993, New Orleans, LA.

CP-3894-2A

1 mm
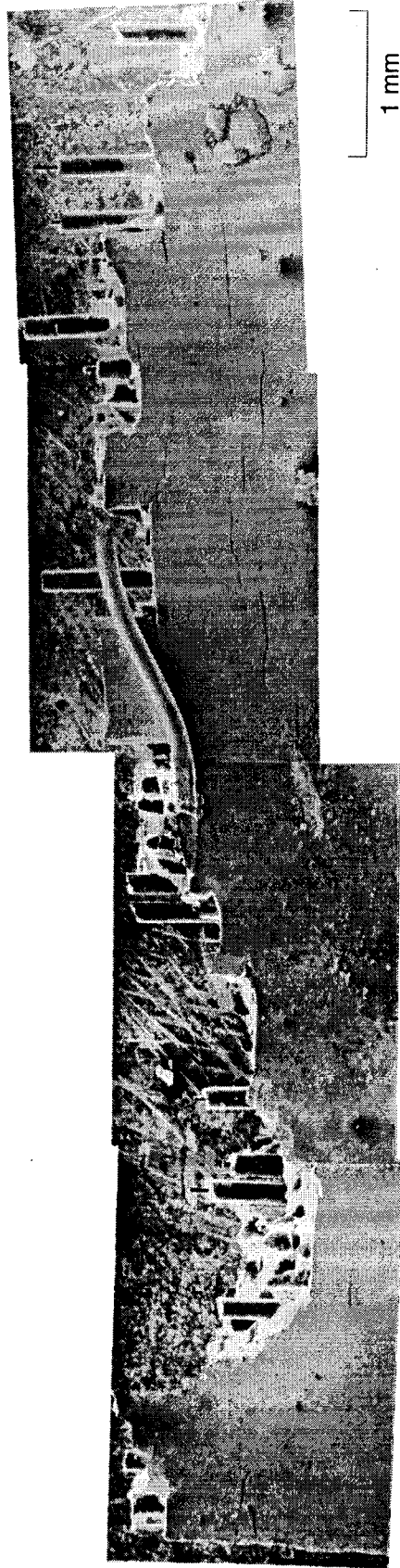
Figure 3.2. Side view of fracture surface.

evident. The ultimate fracture surface appears to result from the linking of parallel thermo-mechanical fatigue cracks by shear cracks. Dimensions of the heights of the sheared regions were measured from Figure 3.2. The sheared area estimated from these measurements was 0.833 mm^2. We estimated the maximum shear stress to be the maximum tensile stress divided by $\sqrt{3}$ which, when multiplied by the sheared area, results in a load estimate of 52 kg.

We estimated the load supported by friction between the broken fibers and the matrix by measuring the total length of exposed fiber on the fracture surface shown in Figure 3.2 and doubling that value to account for exposed fibers on the conjugate fracture surface. Using the diameter of the fibers (140 µm), the area of the exposed fiber/matrix interface was computed to be 7.59 mm^2. An estimate for the interface shear strength of 150 MPa was obtained from measurements by Warren, Mackin, and Evans[12] for prefatigued Ti-15-3/SCS-6 composite. Based on their estimate for the interface shear strength, we computed the load from friction between broken fibers and the matrix to be 116 kg.

Figure 3.3 shows the estimated contribution of each of the four sources of residual strength. The contribution of the fibers is roughly equal to the matrix, and the shear mechanisms (i.e., shear of the matrix between fatigue cracks and shear of the matrix/fiber interface) were responsible for less than one-fourth of the total residual strength.

The sum of the estimated contribution of the four sources or residual strength is 630 kg, which is less than the maximum applied load of 785 kg. Perhaps the greatest uncertainty in the estimated loads comes from the estimate of the number of fibers that broke during thermomechanical fatigue. If crack bridging occurred, unbroken fibers in the region of fatigue cracking (i.e., the flat matrix fracture surface area) would have contributed to the residual strength. Assuming crack bridging is the reason for the difference between the estimated load and the maximum applied load, an additional 27 fibers would need to be unbroken in the region of the flat matrix cracking.

As mentioned above, only those fibers that were completely surrounded by ductile matrix failure were assumed to contribute to the residual strength. Examination of Figure 3.1 revealed that 61 fibers are partially in contact with the ductile matrix failure region. If half of these fibers were unbroken (about 30), the estimated residual strength would be 793 kg, which is in good agreement with the maximum applied load (785 kg).

---

[12] P. D. Warren, T. J. Mackin, and A. G. Evans, "Design, Analysis, and Application of an Improved Push-Through Test for the Measurement of Interface Properties in Composites," Acta Metall., **40**, 1243 (1992).
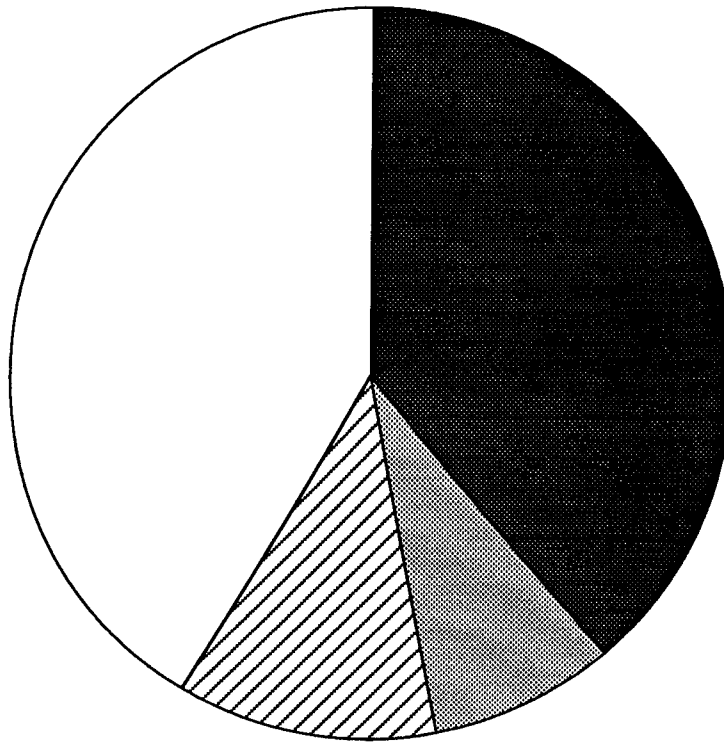
Total Calculated Load   =   630 kg
Maximum Applied Load   =   785 kg

☐ 260 kg Load from Fibers in
     Ductile Fracture Region

■ 244 kg Load from Ductile Matrix
     Fracture Region

▨ 52 kg Load from Shear Fracture
     Region

▧ 74 kg Fiber/Matrix Friction Load

CAM-3894-3A

Figure 3.3.   Estimated contributions to the residual strength.

28

This work provides an improved understanding of how load bearing capacity is partitioned in the microstructure (matrix and fibers) of metal matrix composites. This understanding enables us to make more reliable estimates of the residual strength of damaged metal matrix composite components.

3.3   SUMMARY

This analysis indicates how the load bearing capacity is partitioned across the components of a metal matrix composite in the final stage of failure from thermomechanical loading. We estimated the residual strength of a thermomechanically fatigued Timetal 21S/SCS-6 specimen from a quantitative fracture surface analysis. That analysis showed that the contribution to the residual strength from the fibers and the matrix was approximately equal. About three-fourths of the estimated residual strength was attributed to tensile failure of the matrix and the fibers. The remainder was from shear failure in the matrix and matrix/fiber interface sliding.

SECTION 4

DEFORMATION AND FAILURE BEHAVIOR OF SCS-6/TIMETAL 21S UNDER MULTIAXIAL LOADS: EXPERIMENTS

4.1 INTRODUCTION

Metal matrix composites like other fiber composites, are very strong under a uniaxial load in the longitudinal fiber direction. However, tests on composites have shown that biaxial or triaxial loads can produce failure at stresses well below the on-axis failure loads. In most applications, the MMC part will be subjected to biaxial or triaxial stress states. However, there exists little or no information on the strength and behavior of metal matrix composites under multiaxial loading; most of the test data has been obtained on simple test coupons loaded in uniaxial tension. Testing under multiaxial loads is very important for development and validation of damage and failure criteria that can be used in the design of MMC parts. A goal of this ongoing research program is to develop a good set of material charaterization data for SCS-6/Timetal 21S MMC under biaxial loads.

The preliminary material characterization was performed using off-axis tests. These off-axis tests use simple uniaxial loading applied to standard composite tensile coupons, with the modification that the fiber direction in the specimens is oriented at various angles to the coupon loading axis. As a result, the composite is loaded with a combination of longitudinal, transverse, and in-plane shear stresses, which can be determined from a coordinate transformation of the applied uniaxial load.

The off-axis test is an attractive characterization test because it is easy to perform and analyze, requires only standard material testing procedures and equipment, and is relatively inexpensive. The test also allows inspection of the specimen edges at intermediate loads so that information about damage development can be obtained. This is not possible with some testing configurations (such as biaxial tests) where the loaded gage section of the specimen has no edges. The limitation of the off-axis tests is that the possible load combinations are determined by the off-axis transformation of the uniaxial load. Thus, the various components of the applied load cannot be independently controlled. As a result, data for characterization of the failure mechanisms can be improved by the addition of biaxial testing.

The following section describes the initial off-axis material characterization tests performed in Phase 1 of this program. In Phase 2, we will concentrate on measuring the behavior under biaxial loads using cruciform specimens. The complete set of material characterization data will be reported after we complete Phase 2.

4.2 OFF-AXIS TENSILE TEST RESULTS

We performed the preliminary set of material characterization, off-axis, tensile tests on the Timetal 21S reinforced with SiC SCS-6 fibers. These tests consisted of a uniaxial loading applied to tensile coupons with fibers oriented at 0°, 15°, 22.5°, 30°, 45°, 60°, and 90° to the specimen axis. The tests produced higher than expected ductility, with the failure strain of the 45° and 30° specimens greater than 2%. These are significantly higher failure strains than those reported for off-axis tests on SCS-6/Ti-6-4 MMC,[13] where failure strains for all specimen orientations are less than 1%. The SCS-6/Ti-6-4 measurements of transverse ductility were consistent with existing measurements for SCS-9/Timetal 21S data.[14] The measurements from these two material systems led us to expect failures for the SCS-6/Timetal 21S studied in this program at or below approximately 1%. We are still investigating the microstructural characteristics of the MMC that lead to the enhanced ductility with measured failure strains greater than 2% for some orientations.

Figure 4.1 shows typical off-axis, stress-strain behaviors measured for the SCS-6/Timetal 21S. Extrapolation of the stress-strain curves to the ultimate failure point was required for some tests as a result of premature strain gage failures that occurred with the higher ductility. The extrapolated portions of the curves are indicated by the dotted lines in Figure 4.1. In all cases shown, the strain gages remained attached to within 8% of the ultimate failure stress. We have modified the strain gage application process to eliminate this problem in future tests. Inspection of the stress-strain curves shows that loading transverse to the fiber direction produces a clear three-stage response that results from the deformation mechanisms of initial elastic response, fiber-matrix debonding, and matrix plasticity, respectively.[15] The off-axis curves also show a lower strength for the 60° orientation than for the 90° orientation, illustrating the importance of shear stress on damage and strength.

[13]Sun, C.T., Chen, J.L., Sha, G.T., and Koop, W.E., "Mechanical Characterization of SCS-6/Ti-6-4 Metal Matrix Composite," J. Composite Materials, 24, 1029-1059 (1990).

[14]Bearden, K.L., 1993, "Behavior of a Titanium Matrix Composite under Quasi-static Tensile and Compressive Loading," M.S. Thesis, Air Force Institute of Technology, AFIT/GAE/ENY/92D-07.

[15]Majumdar, B.S., and Newaz, G.M., "Inelastic Deformation of Metal Matrix Composites: Plasticity and Damage Mechanisms," Phil. Magazine A, 66(2), 187-212 (1992).
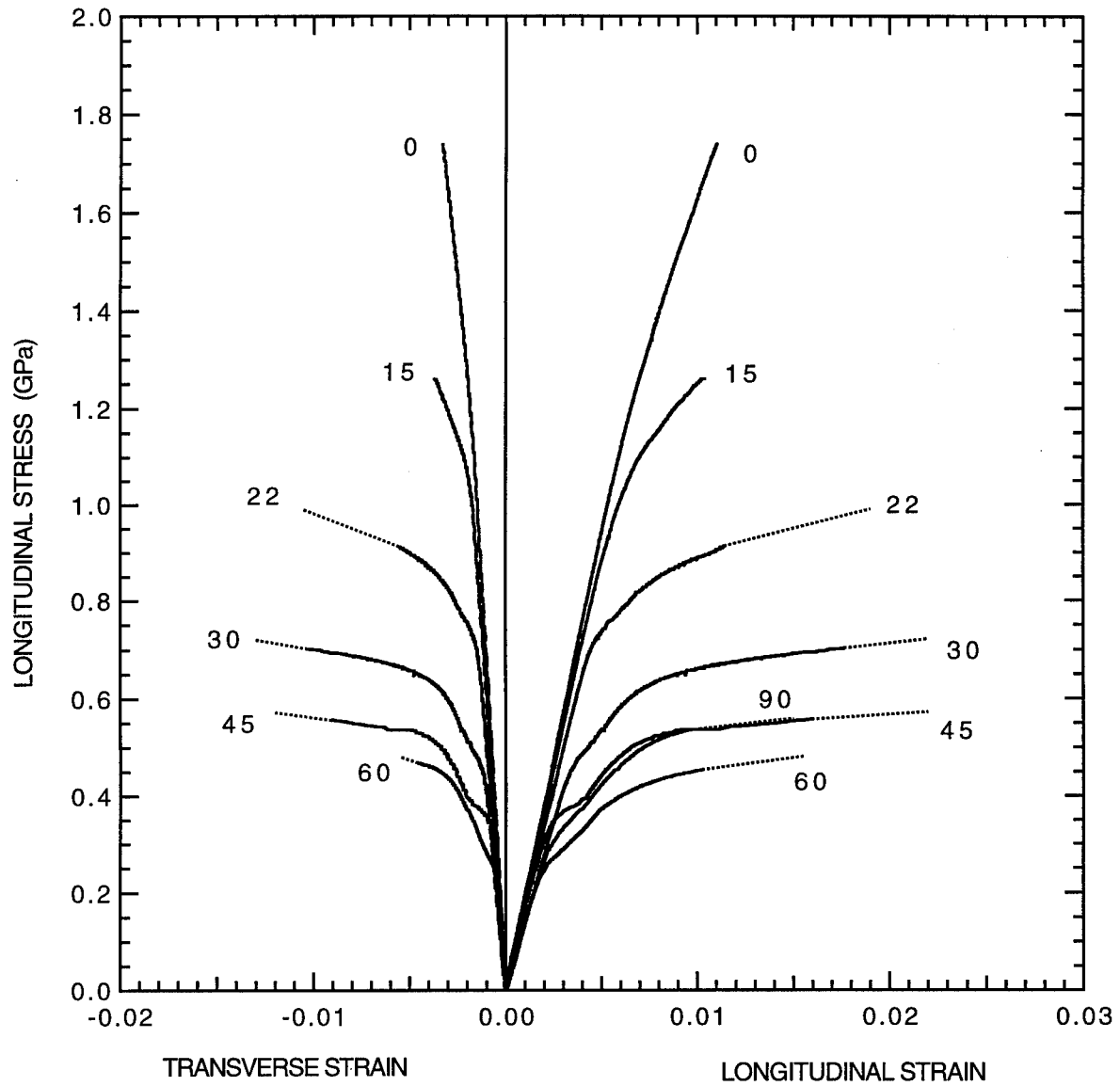
Figure 4.1.   Measured stress-strain behaviors for the SCS6/Timetal 21-S off-axis tensile tests.

We used SEM and conventional metallography to establish the nature and extent of the damage in the specimens. The dominant failure mechanisms were fiber failure at the 0° and 15° orientations, matrix failure at the 30° through 90° orientations, and combined failure mechanisms at 22.5°. We used the replica film technique to observe the damage at various stages of the loading process on the polished edge of selected specimens. The replicas clearly show the failure and tensile opening of the fiber matrix interface in the 90° specimen in the nonlinear region of the stress-strain behavior.

SECTION 5

DEFORMATION AND FAILURE BEHAVIOR OF SCS-6/TIMETAL 21S UNDER MULTIAXIAL LOADS: MODELING

5.1 INTRODUCTION

Two approaches are commonly used to develop damage dependent constitutive models. The first is the phenomenological or macromechanical approach, which develops the constitutive behavior based on measurements of material behavior on dimensions that are large compared to the asperities. The second approach is the micromechanics approach, which performs analyses that account for the microstructural inhomogeneities and deformation mechanisms, such as produced by fibers and damage.

Formulation of a suitable, microstructural, model framework for MMCs requires an understanding of the microstructural deformation mechanisms. The advantage of this microstructural approach is that, once completed, the model can yield a significant amount of insight and information about the microstructural damage processes. This information can be used to design improved material microstructures and to guide the use of the material in structural design. As a result, we have concentrated on microstructural models in this program. The key to development of microstructural models for MMCs is to include sufficient analyses to allow a physically accurate description of the microstructural deformation processes and exclude parameters that are not essential to characterizing material behavior. The necessary microstructural processes that are essential to describing the behavior of SCS-6/Timetal 21S MMC include gradients in stress and strain within the matrix around the fibers and damage and separation of the fiber-matrix interface.

A goal of this research program is to create models that describe the deformation and failure behavior of the SCS-6/Timetal 21S composite under general load conditions. Our work focused on two areas: (1) the application of the "generalized method of cells" originally conceived by J. Aboudi and others[16,17] as a baseline model for comparison and evaluation, and (2) the

[16]Aboudi, J., "Closed Form Constitutive Equations for Metal Matrix Composites," Int. J. of Engineering Science, 25(9), 1129-1240 (1987).

[17]Paley, M., and Aboudi, J., "Micromechanical Analysis of Composites by the Generalized Cell Model," Mechanics of Materials, 14, 127-139 (1992).

35

development of a new, micromechanical, constitutive model capable of describing the damage and failure processes in the MMC. The model under development is three-dimensional and incorporates explicit descriptions of fiber and matrix in separate cell regions, but differs from the generalized method of cells in that weighted equilibrium between cells is used to more accurately model stress concentrations about the fibers with fewer cells. We are developing the model in a manner that is consistent with use in an explicit finite element code where computational efficiency in the constitutive model is important. A description of the method of cells model is given below. The model development in this research program is ongoing and will be described in a future technical report.

5.2 GENERALIZED METHOD OF CELLS MODEL

5.2.1 Introduction

The method of cells, originally conceived by J. Aboudi and others,[16,17] is a micromechanical model that characterizes the composite as consisting of a unit cell that is divided into four subcells—a fiber cell and the three matrix cells. The unit cells are embedded in a doubly periodic array so that the behavior of the unit cell can be used to assess the behavior of the entire composite. A homogeneous state of stress or strain can be applied and the response can be monitored (1) in terms of macroscopic or effective properties of the composite, and (2) in terms of the microscopic behavior of each subcell.

The method of cells has been extended to what is called the generalized method of cells,[18,19] which enables more than four rectangular subcells to be included in the unit cell, the inclusion of an interfacial region, modeling of porosity or damaged regions, modeling of variations in the fiber shapes and arrays, and modeling of the thermomechanical response of the composite.

Early in this effort, we independently developed a computational capability to apply the method of cells; however, more recently, we have redirected our approach to make use of the computational tools being developed by researchers at the University of Virginia.[20,21]

---

[18]Aboudi, J., "Micromechanical Analysis of Composites by the Method of Cells", Appl. Mech. Rev., **42**, 193-221 (1989).

[19]Aboudi, J., *Mechanics of Composite Materials: A Unified Micromechanical Approach*, Elsevier, Amsterdam, 1991.

[20]Aboudi, J. and Pindera, M.-J., Micromechanics of Metal Matrix Composites Using the Generalized Method of Cells Model (GMC) User's Guide, NASA Contractor Report 190756 (October 1992).

[21]Mirzadeh, F. and Herakovich, C. T., "Graphical User Interface (GUI) for the Response of Composite Materials," Report prepared under VCIT Grant MAT-94-006, August 17, 1994.

5.2.2 Model Performance

Two aspects of the mechanical behavior of unidirectionally fiber reinforced SCS-6/Timet B21S composite were simulated as follows: (1) the method of cells was used to simulate the yield stress under biaxial loading, and (2) the generalized method of cells was used to simulate the nonelastic, uniform, stress-strain behavior under loading in the [0] and [90] orientations. In our first simulation, we used the method of cells to predict the yielding behavior of unidirectionally fiber-reinforced SCS-6/Timet B21S composite under biaxial loading. Figure 5.1 shows the cell pattern that was used and Figure 5.2 shows the stresses present in each subcell when the effective stress in one of the matrix subcells reaches the yield. The material is oriented so that the fibers are aligned in the x_1 direction and the biaxial stresses are applied in the x_1-x_3 plane. Residual stresses from material processing are not included in this analysis. Two yield criteria are shown in Figure 5.2, one based on the maximum effective matrix subcell stress and the other based on the average effective matrix subcell stress. Pindera and Aboudi[22] compared these yield criteria to finite element solutions and found good agreement with the maximum effective matrix subcell stress criterion.

The subcell stresses indicate that the location of initial yielding varies with stress state. When the in-plane principal stresses are both tensile or compressive and the higher stress is in the fiber direction (x1), yielding initiates in Subcell 3. Yielding initiates in Subcell 2 in all other biaxial stress states. The only exception is when the nonzero principal stress is collinear with the fibers, which causes all matrix subcells to yield simultaneously.

These results demonstrate the capability of the method of cells to simulate the macro and micromechanical response of the B21S/SCS-6 composite under biaxial loading. Verification of the results from the method of cells will be obtained from a comparison with experimentally observed yield trends and detailed finite element analysis results from the follow-on study.

In our second simulation, we used the generalized method of cells to characterize the effect of thermal stresses and fiber/matrix bond strength on the tensile behavior of the composite. Figure 5.3 shows the effect of thermal stresses on the room temperature tensile behavior. The thermal stresses, in this case, are induced in the composite during cool down from 760°C in the final manufacturing step. Figure 5.3 shows that, for a 0° composite orientation, the yield strength is reduced from about 2.0 GPa to 1.6 GPa. Tensile longitudinal stresses in the matrix are responsible for decreased yield. For the 90° orientation, the residual stresses slightly increase the composite stiffness immediately after the yield because of compressive residual stresses in the matrix in the directions between nearest neighbor fibers. This example assumes, somewhat

---

[22]Pindera, M.-J. and Aboudi, J., "Micromechanical Analysis of Yielding of Metal Matrix Composites," Int. Jour. of Plasticity, **4**, 195-214 (1988).
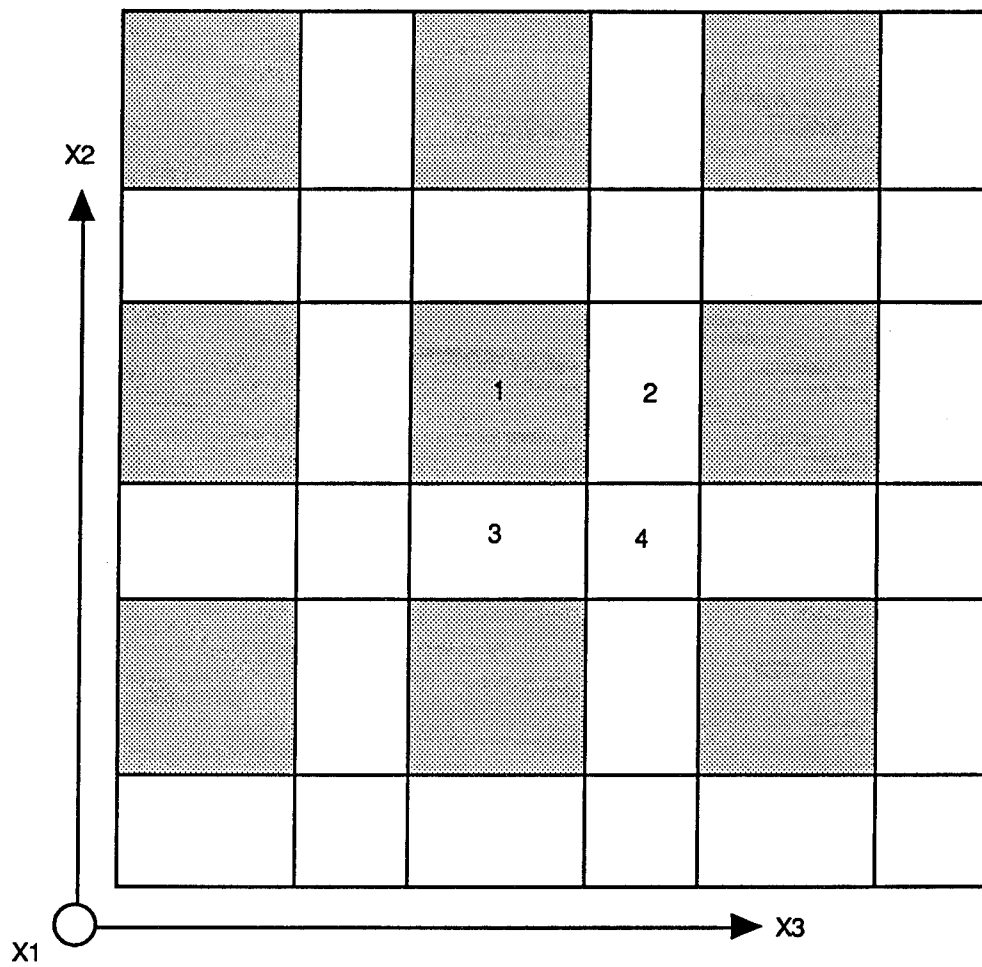
Figure 5.1.   Subcell pattern for the generalized method of cells simulations
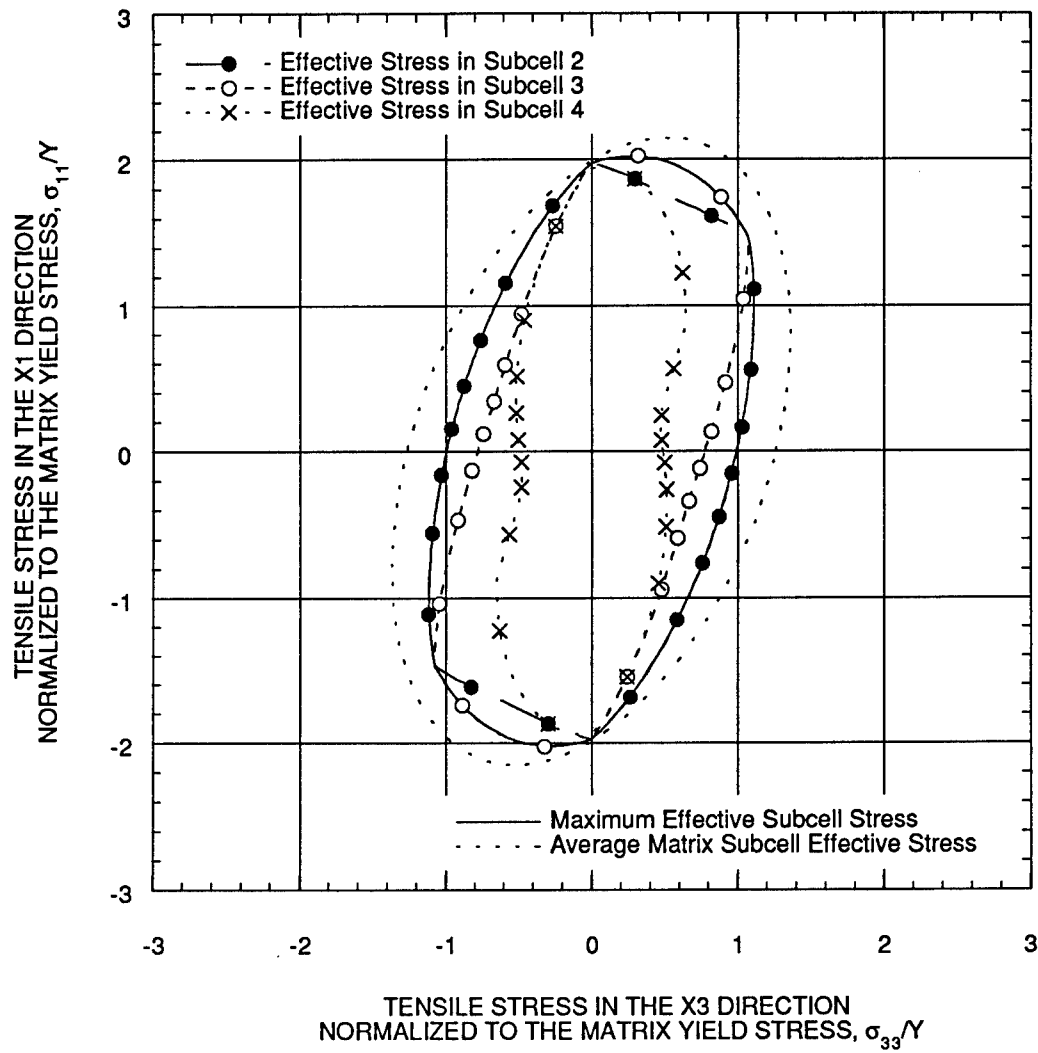of SCS6/Timetal 21-S composite.

Figure 5.2. Method of cells simulation of the yield stress of SCS6/Timetal 21-S composite.
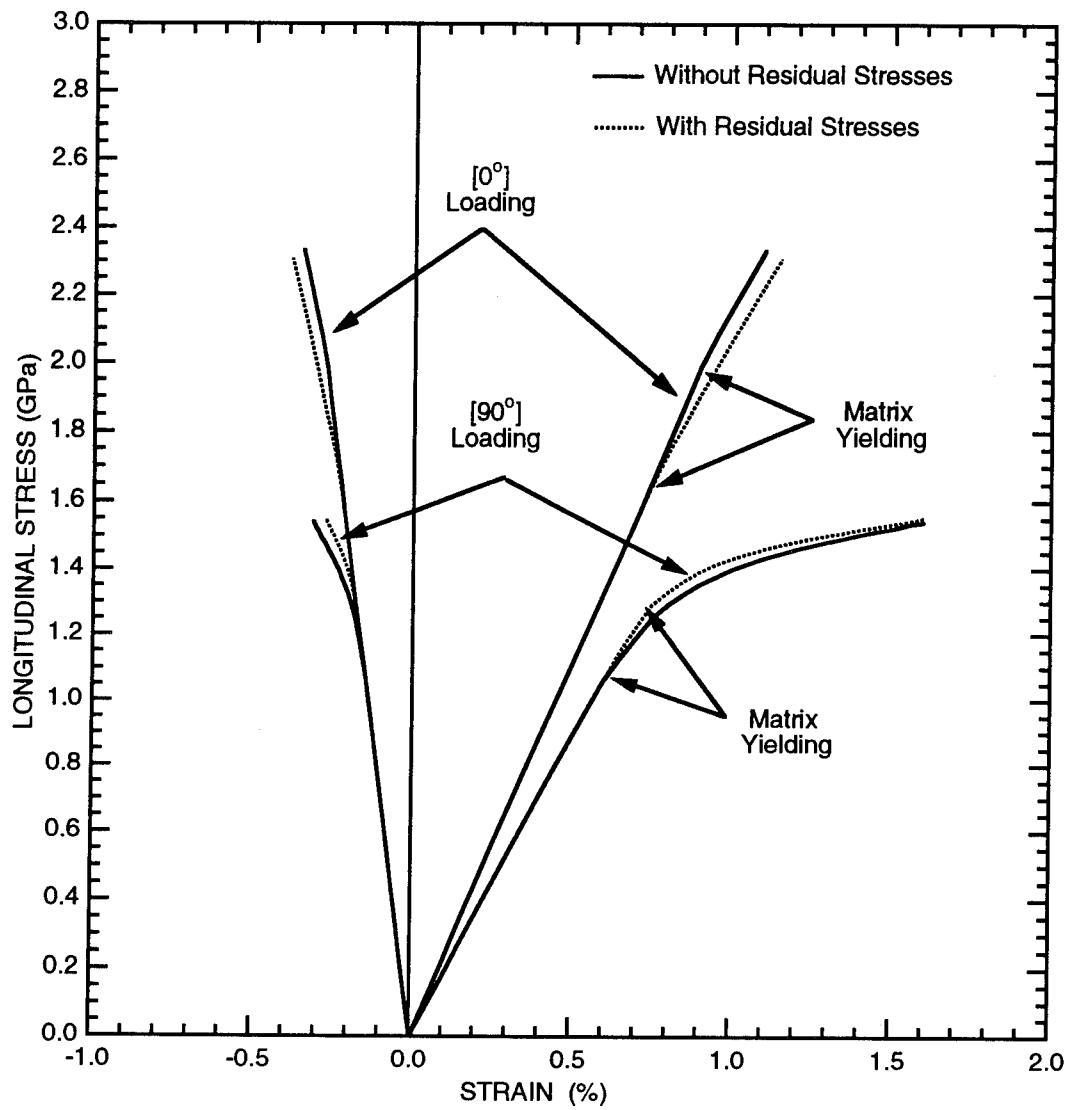
Figure 5.3. Generalized method of cells simulations of the effect of thermal residual stresses on the behavior of 0° and 90° SCS6/Timetal 21-S, assuming perfectly bonded fibers.

40

inappropriately for the composite of present concern, that bonding between the fiber and matrix is perfect.

In Figure 5.4, the longitudinal stress in the individual subcells of the model are shown for the 90° loading conditions shown in Figure 5.5. The figure shows that perfect fiber/matrix bonding increases strength and stiffness, because most of the load is borne by the matrix subcells (such as subcell 3 shown in Figure 5.4) that are collinear with the fiber (subcell 1) in the direction of the applied load. Without fiber/matrix bond strength, the overall strength of the composite is greatly reduced, because the stress bearing regions are limited to subcells between the fibers (subcells 2 and 4), which do not benefit from the higher strength fibers.

Figure 5.5 shows the sensitivity of the stress-strain behavior to the fiber/matrix bond strength. In the 0° composite, interfacial bond strength has no effect on the longitudinal stress-strain behavior, although, in the transverse direction, weakening the bond strength slightly reduces the stiffness. For the 90° orientation, lack of bonding reduces the yield and the stiffness by about a factor of three. A comparison between the calculated behavior for the 90° orientation and the measured behavior indicates that the unbonded fiber assumption is a better representation of the actual behavior than the perfectly bonded fiber assumption.

5.2.3 Summary

The generalized method of cells results show substantial sensitivity of the yield to fiber/matrix bonding, especially under 90° loading. Furthermore, the generalized method of cells shows that residual stresses resulting from the cool down after fabrication lower the yield for 0° loading and slightly increase the yield under 90° loading. These trends are in qualitative agreement with expectations and with finite element simulations for the comparisons made thus far. Thus, the generalized method of cells is able to simulate the basic features of the composite response. Further comparisons are needed to bound the level of accuracy and physical reasonableness of the model.
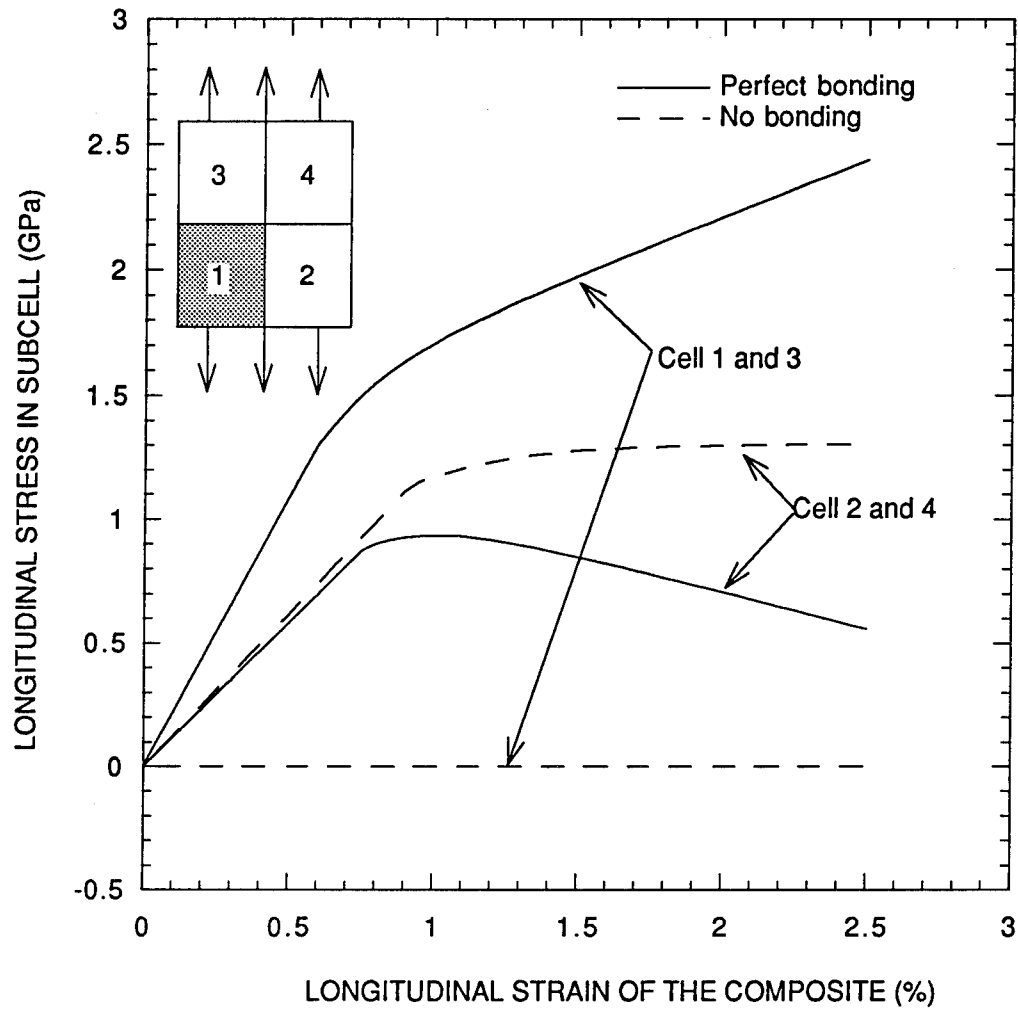
Figure 5.4. Cell response from simulations of the effect of fiber/matrix bonding
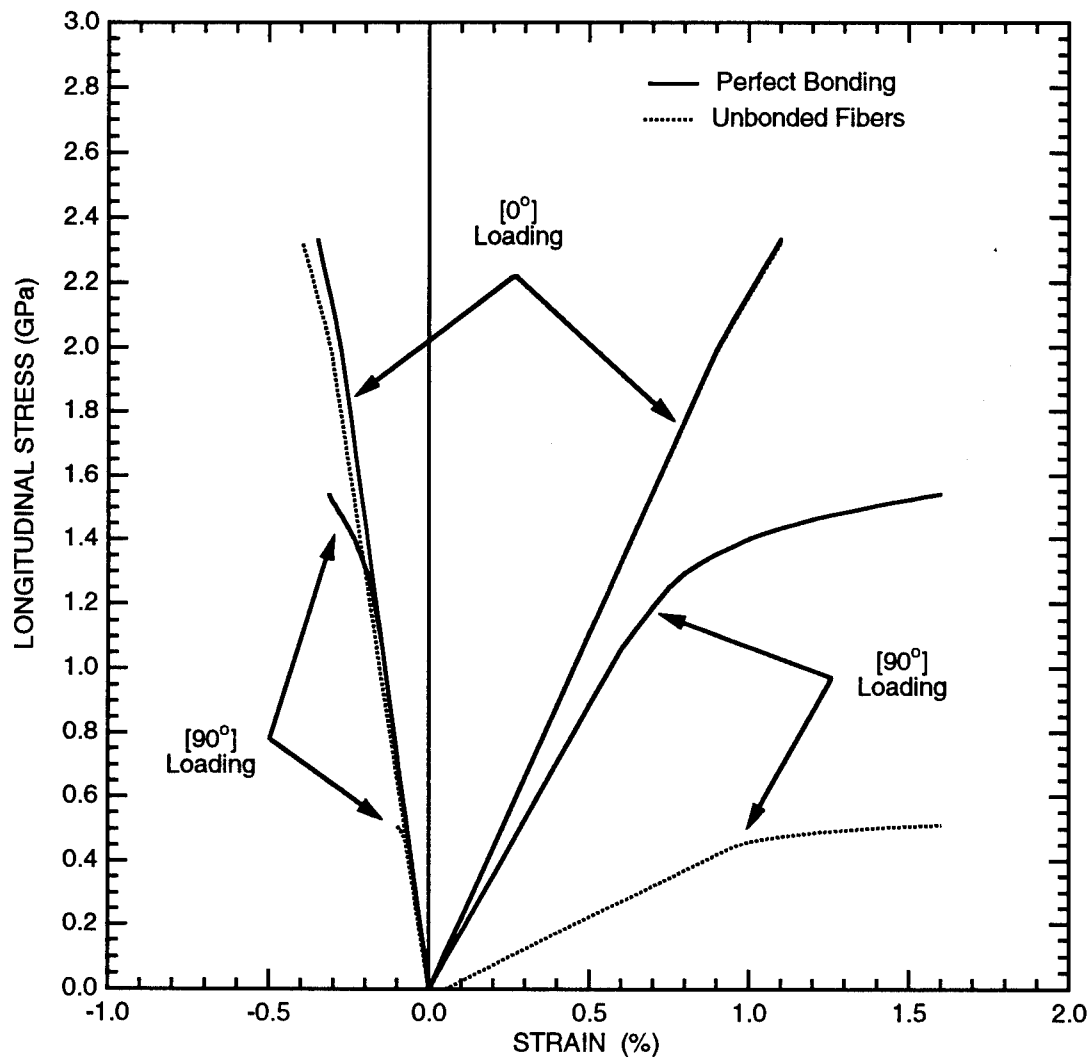in SCS6/Timetal 21-S composite.

Figure 5.5.   Generalized method of cells simulations of the effect of fiber/matrix interface bonding on the behavior of 0° and 90° SCS6/Timetal 21-S without thermal residual stresses.

APPENDIX

THE SEQUENCE OF MICROFAILURE EVENTS
IN A BRITTLE MATRIX COMPOSITE

APPENDIX

THE SEQUENCE OF MICROFAILURE EVENTS IN A BRITTLE MATRIX COMPOSITE

We applied an advanced fractographic technique (FRASTA) to a failed BMC specimen. The goal was to ascertain the sequence of microfailure activity. The specimen, a borosilicate 7040 glass/SiC fiber composite, was supplied by Dr. Nick Pagano and Dr. Rollie Dutton of the Wright Laboratory after it had failed under thermal cycling and superimposed monotonic tension. Figure A.1 shows the complex macrofailure pattern of this specimen. The area examined with FRASTA is indicated.

Figures A.2 and A.3 show contrast images and color-coded elevation images of the two conjugate fracture surfaces as produced by a confocal optics scanning laser microscope. Each image is a montage of four fields of view. Figure A.4 is a perspective topographic view of the conjugate surfaces. A detailed comparison of conjugate topographic features shows surface mismatches in many areas and indicates that many small pieces of material have been liberated from the fracture surfaces during specimen failure.

Figure A.5 shows a series of fractured area projection plots obtained by positioning the conjugate surfaces in their relative configuration at the time of failure. White areas show where the conjugate surfaces are separated; dark areas are in-contact or overlapped areas. The white areas indicate cracks or material lost from the fracture surfaces. The dimensions of the white areas do not change with increasing topograph spacings until a spacing of 0.68 to 0.70 is reached. Figure A.6 shows how the white area increases with conjugate surface spacing.

The nucleation and growth of the white areas at spacings greater than 0.68 in Figure A.5 suggest the fracture process in this composite. Microcracks appear to initiate near the fiber/matrix interfaces and propagate through the matrix. These plots show the rapid propagation of matrix cracks and (relatively) long afterwards the fracture of the SiC fibers.

Figure A.7 shows a fractured area projection plot (FAPP) at the spacing of 0.736. The lines indicate the locations at which the cross-sectional plots were made. Cross-sectional plots were made parallel to the horizontal direction, Figure A.8, and parallel to the vertical direction, Figure A.9. The plots indicate that many areas of the conjugate surface profiles match very well.

Areas where large gaps exist indicate that material was liberated from the fracture surfaces, probably by fragmentation of the matrix material.

Taken together, these results provide a detailed picture of the internal fracture process for this BMC. Correlation among FAPPs, cross-sectional plots, and local microstructures is necessary to establish the fracture mechanisms and governing parameters.
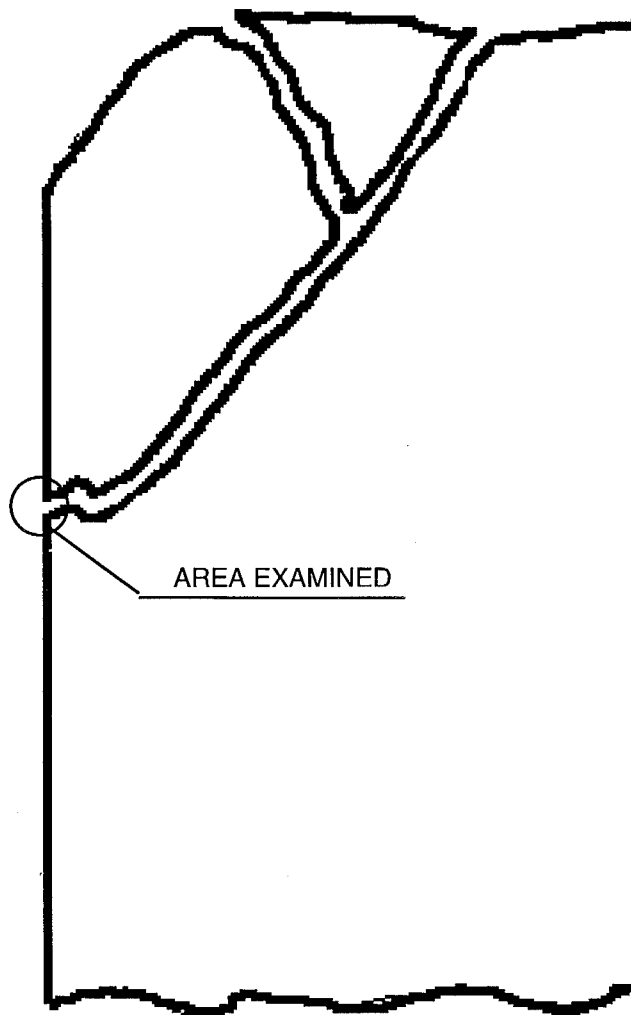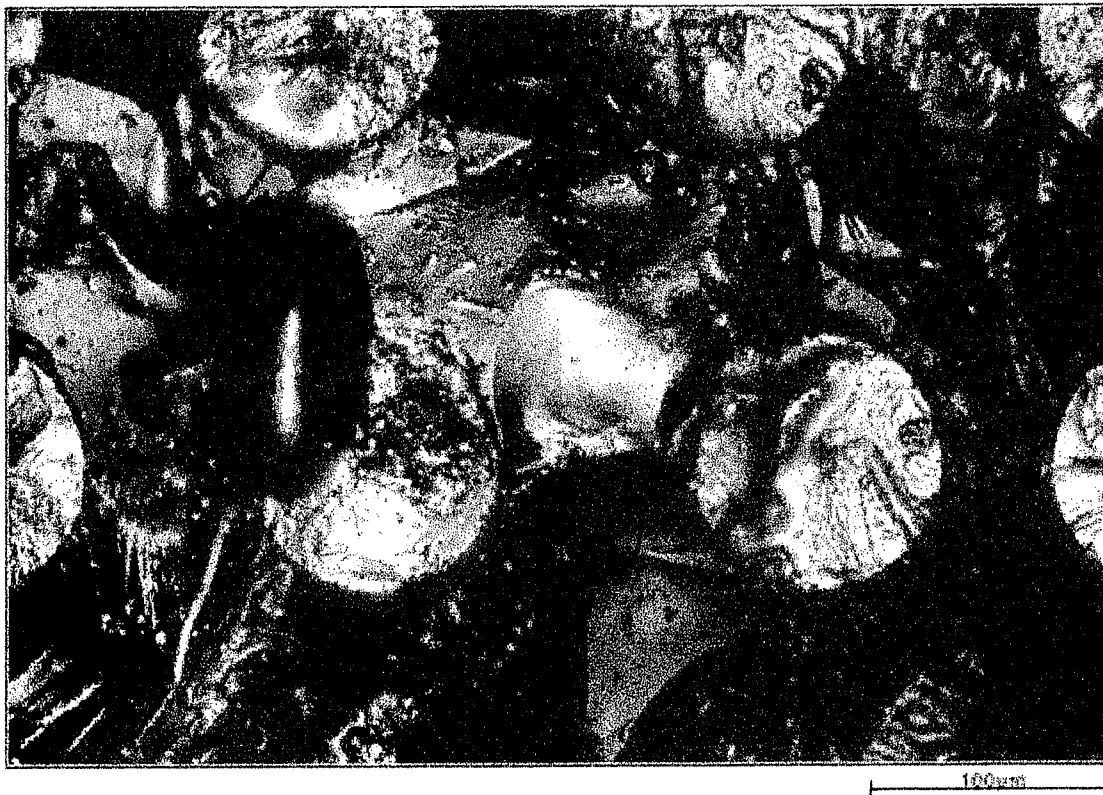
AREA EXAMINED

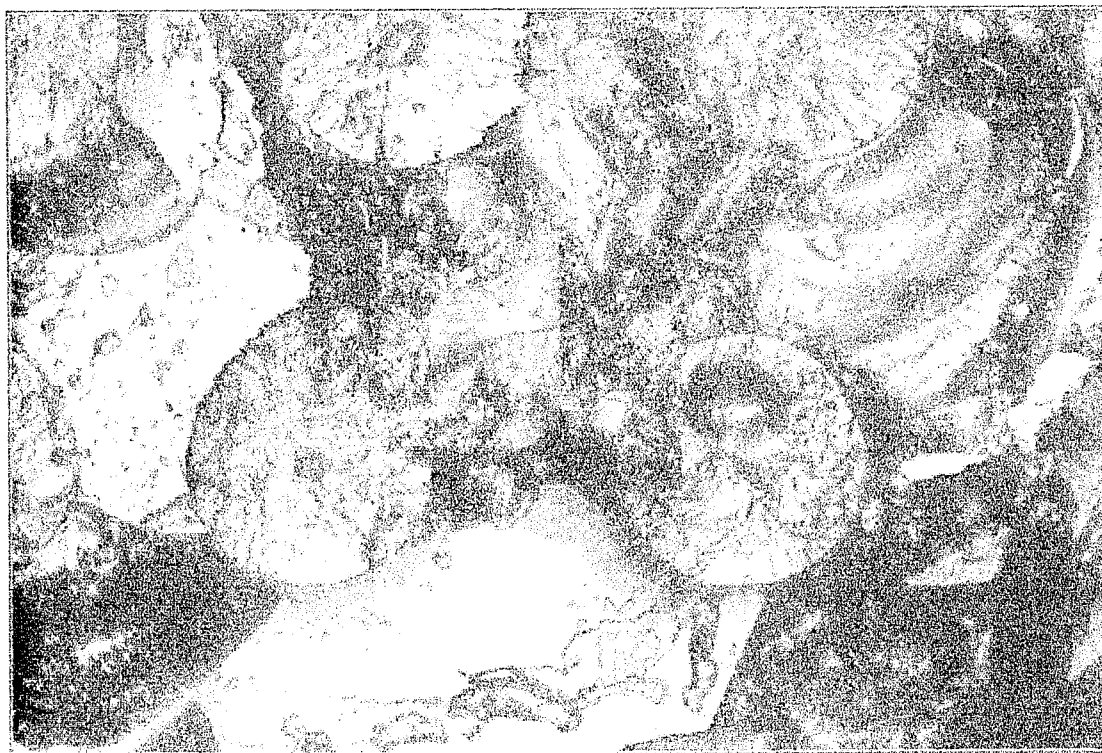Figure A.1. Sketch showing fracture pattern and the location where FRASTA was applied.

(a) Contrast image of Surface A

(b) Color-scale topography image of Surface A

Figure A.2. Contrast and elevation images of Surface A.

(a) Contrast image of Surface B

(μm)

656.51

574.45

492.38

410.32

328.26

246.19

164.13

82.06

0.00

(b) Color-scale topography image of Surface B

Figure A.3. Contrast and topography images of Surface B.
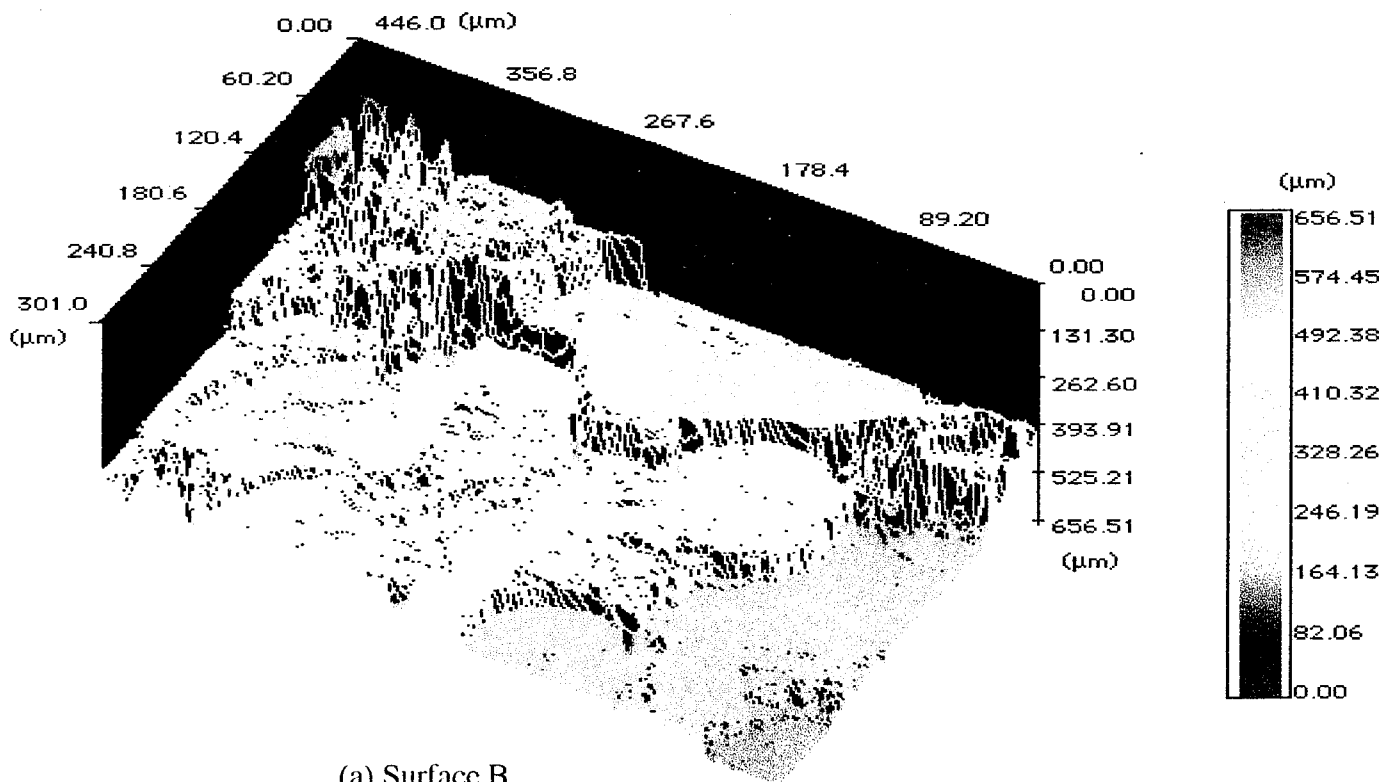
(a) Surface B
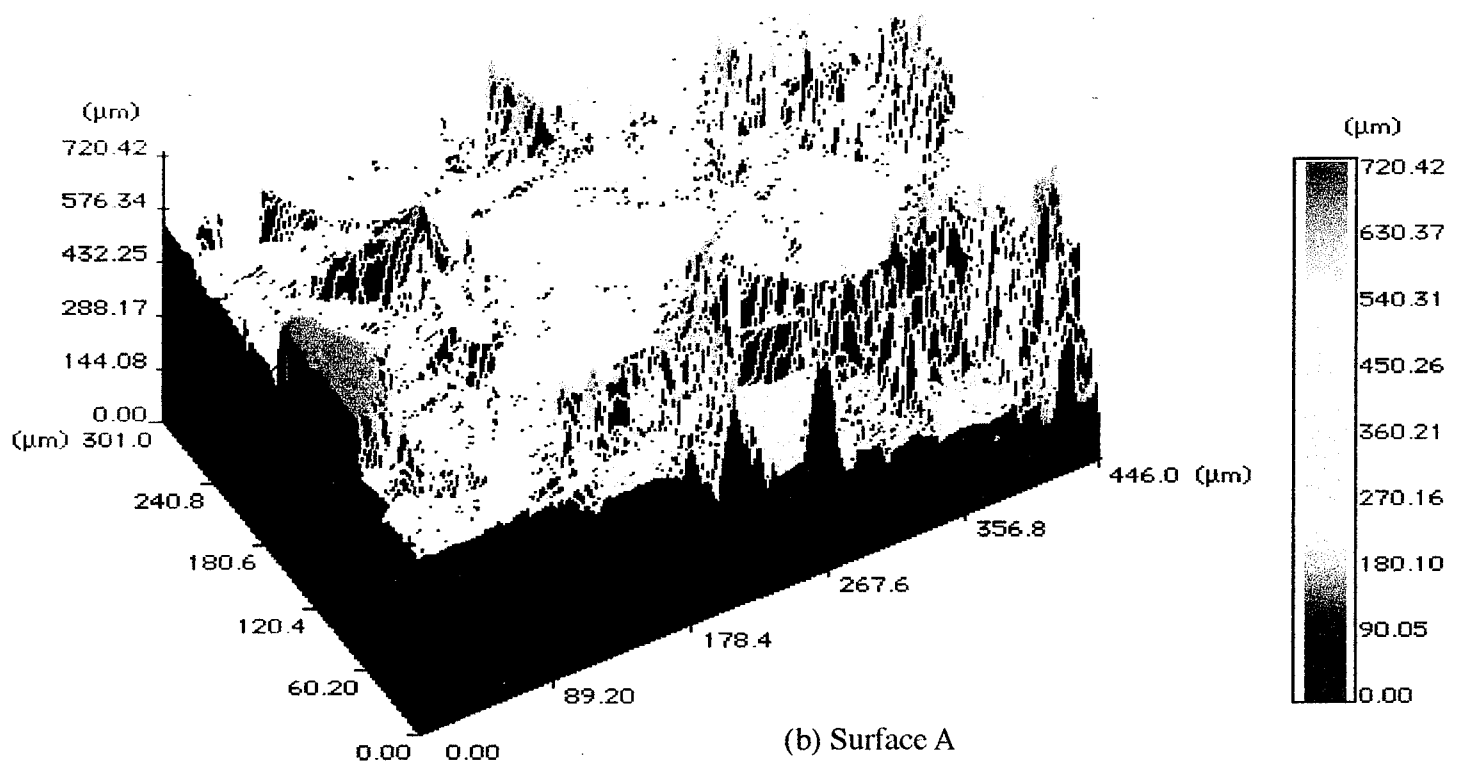
(b) Surface A

Figure A.4. Perspective views of conjugate fracture surfaces.
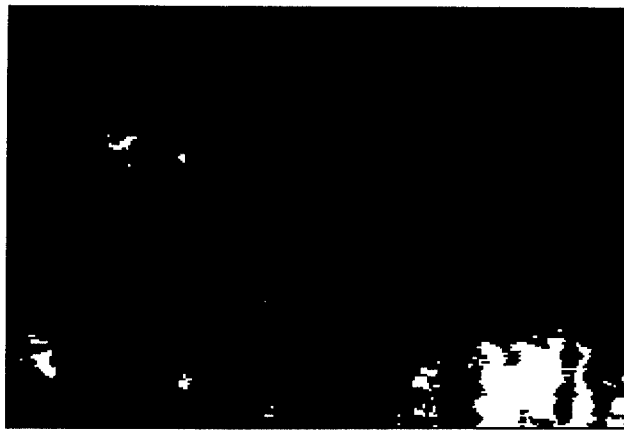
Sep=0.5000(3.92%)
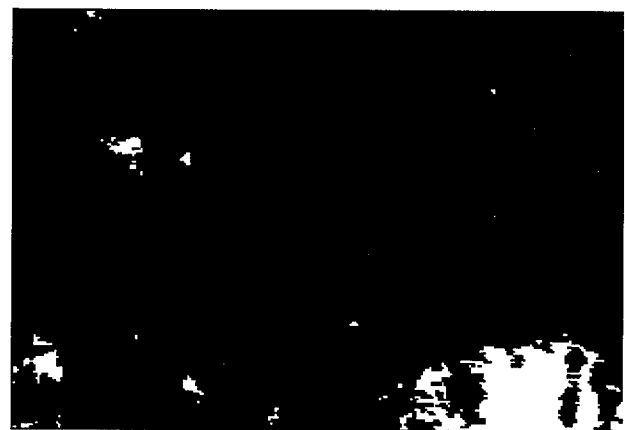
Sep=0.5200(5.39%)
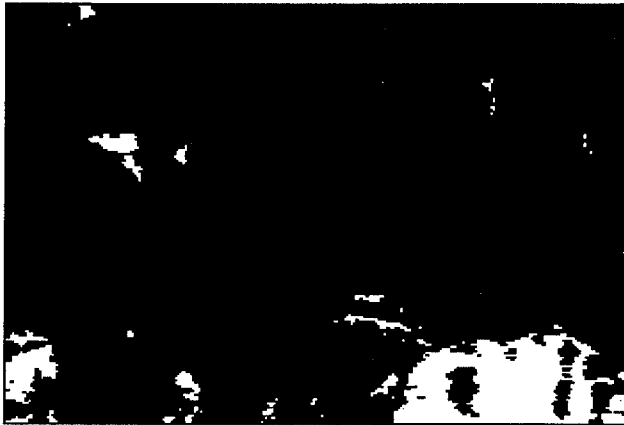
Sep=0.5400(7.72%)

Sep=0.5600(12.08%)
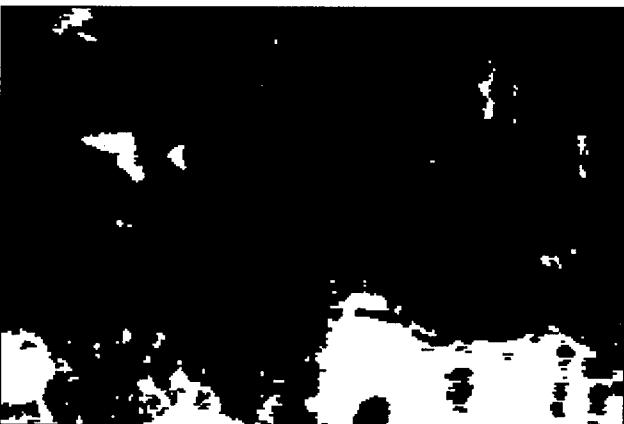
Sep=0.5800(14.39%)

Sep=0.6000(17.11%)

Sep=0.6200(19.93%)

Sep=0.6400(23.07%)

Figure A.5. A series of fractured area projection plots showing microfracture processes inside material.

Sep=0.6600(26.11%)

Sep=0.6800(28.91%)

Sep=0.7000(33.93%)

Sep=0.7100(38.36%)

Sep=0.7200(44.73%)

Sep=0.7300(53.60%)
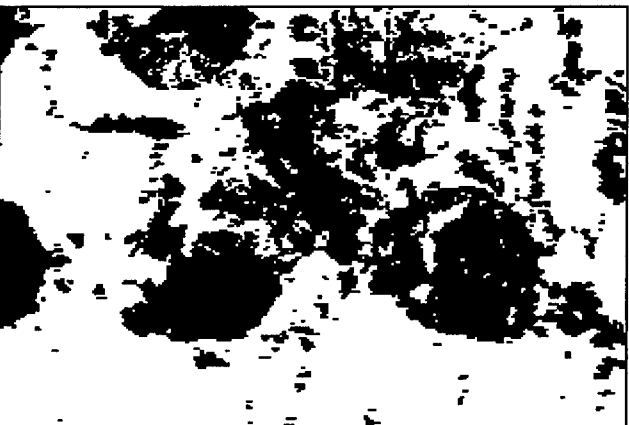
Sep=0.7400(66.69%)

Sep=0.7500(84.19%)

Figure A.5. A series of fractured area projection plots showing microfracture processes inside material (concluded).

A-8
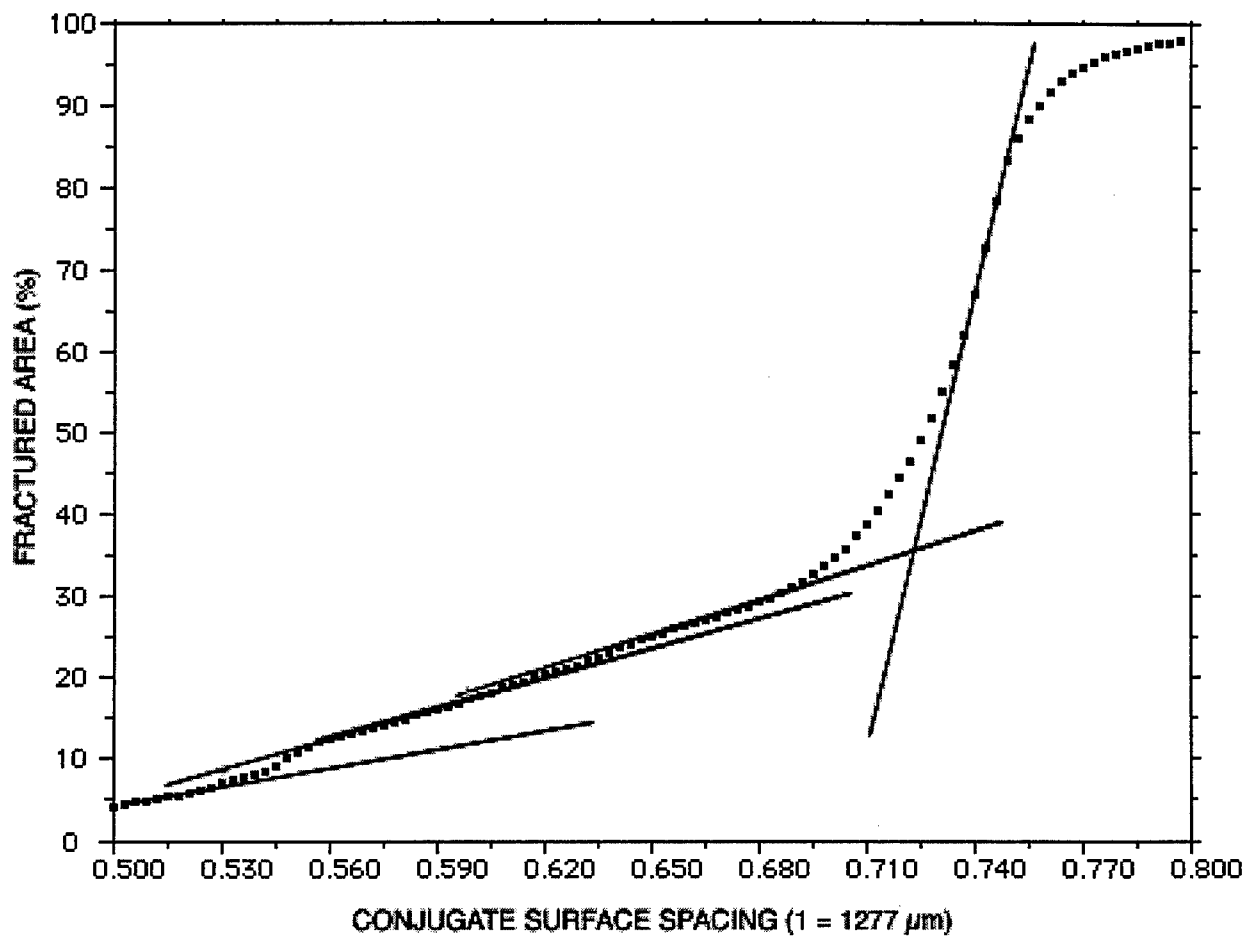
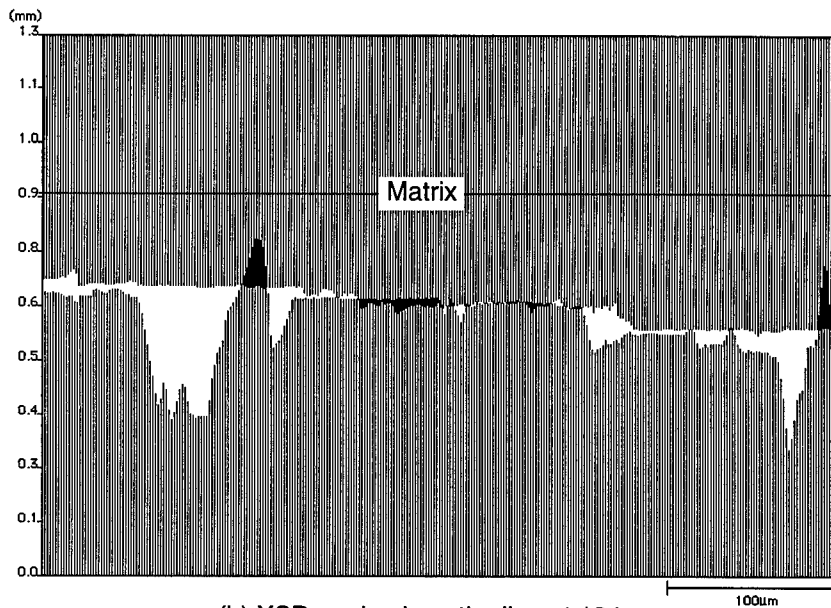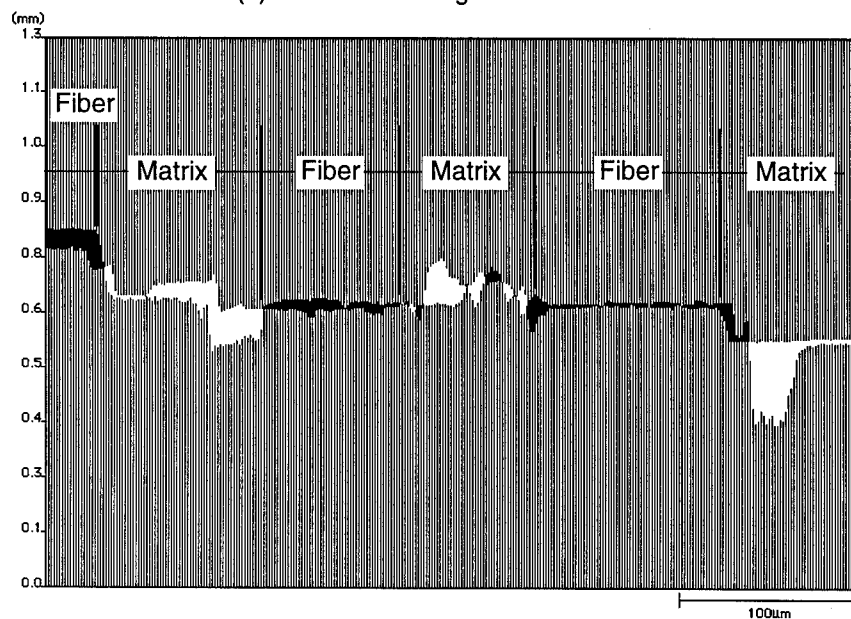Figure A.6. Fractured area increase rate as a function of conjugate surface spacing.
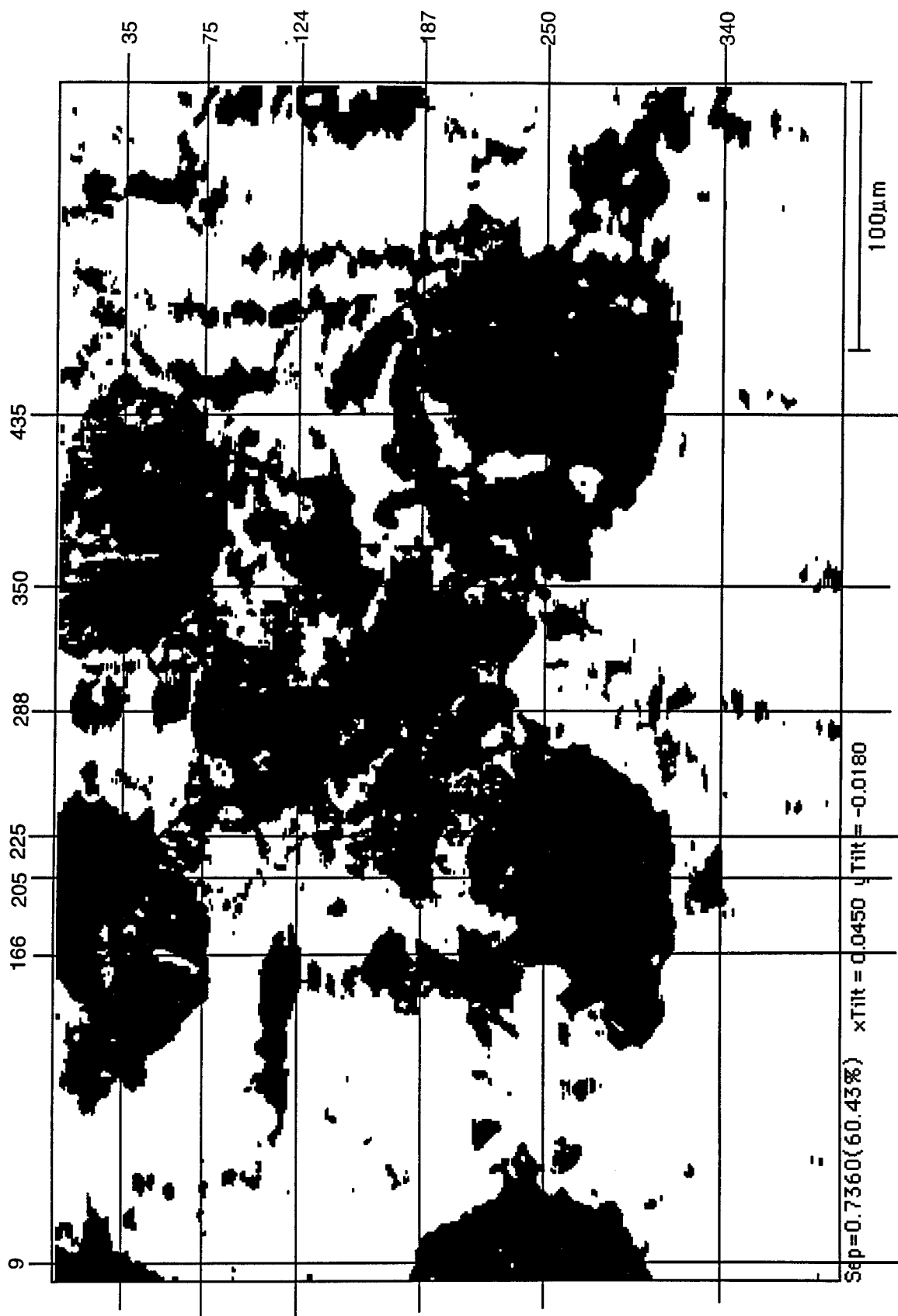
Figure A.7. Fractured area projection plot showing the locations at which cross-sectional plots were made.
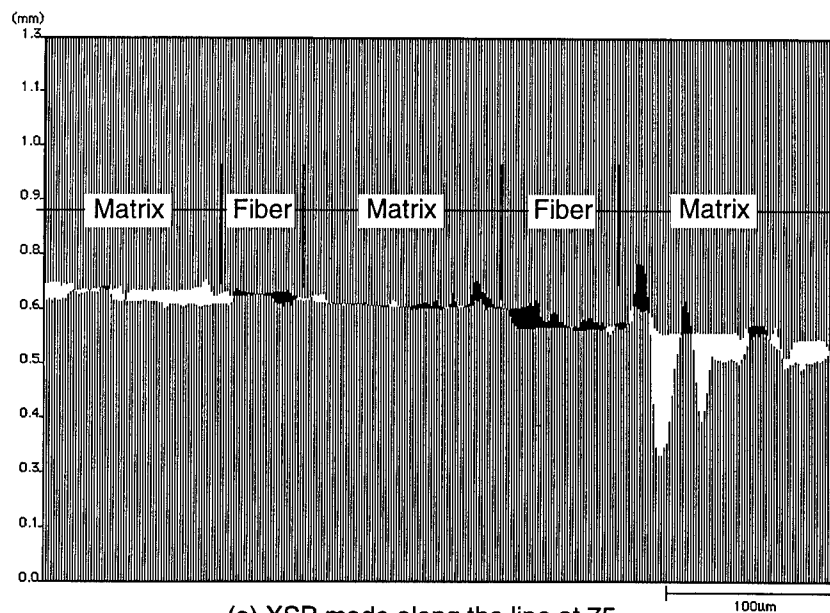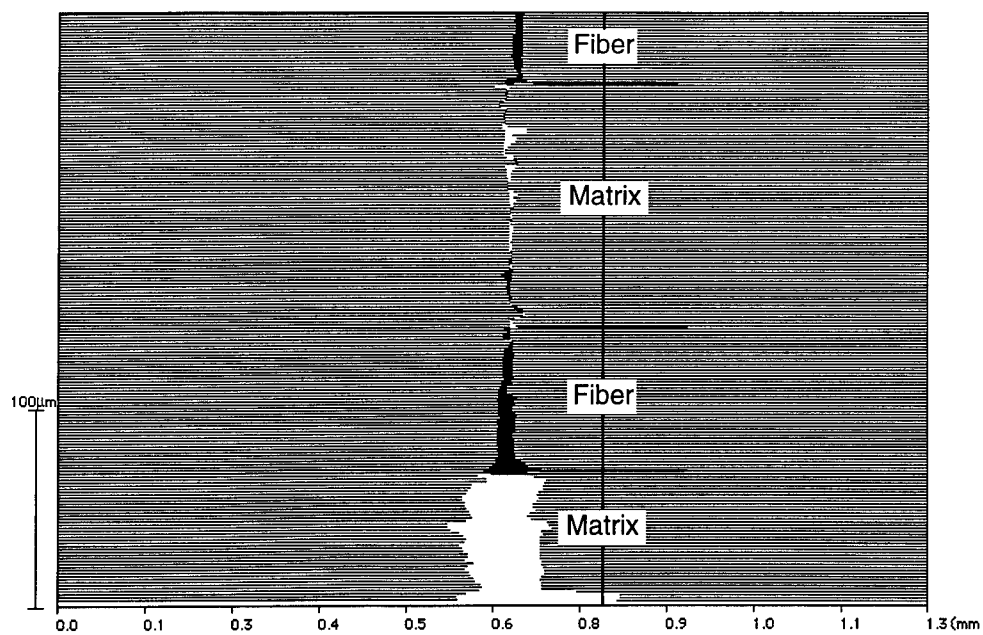
(a) XSP made along the line at 75
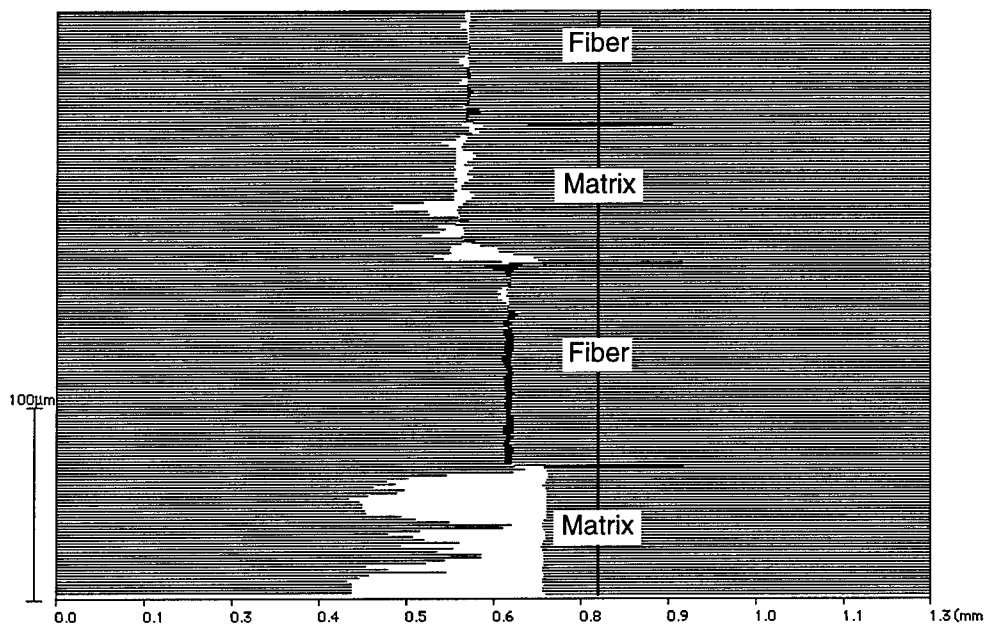

(b) XSP made along the line at 124

(c) XSP made along the line at 250

Figure A.8. Cross-sectional plots made parallel to horizontal direction.

(a) XSP made along the line at 225

(b) XSP made along the line at 435

Figure A.9. Cross-sectional plots made parallel to vertical direction.